Measurement of the Energy Loss of Heavy Ions in Laser-produced Plasmas

Vom Fachbereich Physik
der Technischen Universität Darmstadt

zur Erlangung des Grades
eines Doktors der Naturwissenschaften
(Dr. rer. nat.)

genehmigte **Dissertation** von
Dipl.-Phys. **Renate Knobloch-Maas**
aus Frankfurt am Main

Referent: Prof. Dr. Markus Roth
Korreferent: Prof. Dr. Dr. h.c./RUS Dieter H.H. Hoffmann
Tag der Einreichung: 13.10.2009
Tag der Prüfung: 25.11.2009

Darmstadt 2009
D17

Zusammenfassung

Während der letzten Jahre war der Energieverlust von schweren Ionen in Plasma ein Forschungsschwerpunkt der Arbeitsgruppe Laser- und Plasmaphysik der Technischen Universität Darmstadt. Mehrere Experimente mit lasererzeugten Plasmen wurden bei der Gesellschaft für Schwerionenforschung (GSI) in Darmstadt durchgeführt, da die GSI die einmalige Kombination einer Beschleunigeranlage und des in dieser Arbeit ebenfalls beschriebenen Lasersystems nhelix an einem Experimentierplatz bietet.

Die Experimente konzentrieren sich auf die Messung des Energieverlustes mittelschwerer Ionen in einem Plasma, das durch direkte Heizung einer dünnen Kohlenstoff-Folie mit dem nhelix-Laser bei einer Laserenergie von etwa 50 J erzeugt wird. Da der Energieverlust mit Hilfe einer Flugzeitmessung ermittelt wird, dient ein Stopdetektor zum Aufzeichnen der Ionenpulse, nachdem diese das Plasma und eine 12 m lange Driftstrecke durchquert haben.

Zu Beginn dieser Arbeit wurde klar, daß die zuvor benutzten Detektortypen ihrer Aufgabe nicht gerecht werden konnten; dies wurde im Verlauf dieser Arbeit geändert. Der Stopdetektor muß in der Lage sein, Ionenpulse mit einer Frequenz von 108 MHz und einer Halbwertsbreite von 3 ns bei sehr niedrigem Teilchenstrom zeitlich aufzulösen. Er muß ebenfalls auf den Röntgenpuls aus dem Plasma mit einer Totzeit reagieren, die kürzer ist als die Differenz zwischen der Flugzeit des Röntgenlichts und der Ionen zwischen dem Plasma und dem Detektor. Um diese und andere Anforderungen zu erfüllen, wurde ein neuer Diamantdetektor entwickelt, der seitdem für einige Messungen verwendet wurde. Zusätzlich zu dem neuen Detektor wurden auch die Diagnostik und der zum Heizen der Folie benutzte Laser verändert und verbessert. Das lasererzeugte Plasma erreicht nun eine Maximaltemperatur über 200 eV und eine Dichte freier Elektronen von bis zu 10^{22} cm^{-3}.

Mit diesem stark verbesserten Experimentaufbau konnten Energieverlustdaten mit einer sehr viel besseren Auflösung als zuvor gemessen werden, mit einem Ionenstrahldurchmesser von nur 500 μm. Mit dem neuen Detektor konnten dünnere Folien einer Dicke der Größenordnung 100 μg/cm^2 benutzt werden. Diese Folien werden sehr schnell in völlig ionisiertes Plasma verwandelt. Mit den alten Detektoren mußten dickere Folien verwendet werden, da die Detektoren nicht in der Lage waren, die nötige Auflösung für die dünnen Folien zu liefern. Die neu gemessenen Energieverlustdaten zeigen ein unerwartetes Verhalten. Am Anfang der Laser-Plasma-Wechselwirkung sinkt der Energieverlust zunächst stark, steigt dann wieder auf einen gegenüber dem Energieverlust in der kalten Folie bis zu 30% erhöhten Wert, und sinkt dann wieder langsam weiter ab. Um Erklärungen für dieses Verhalten zu finden, wurden mehrere Änderungen durchgeführt, unter anderem eine Umkehr der Experimentgeometrie, um zu klären, ob Felder für das Absinken des Energieverlusts verantwortlich sein könnten.

Abstract

The interaction of ions with plasma is not yet fully understood today, although it is important for inertial fusion technology. During recent years, the energy loss of heavy ions in plasma has therefore been a subject of research in the Laser and Plasma Physics group of Darmstadt University of Technology. Several experiments were carried out at the Gesellschaft für Schwerionenforschung (GSI) in Darmstadt using laser-created plasma, thereby taking advantage of the unique combination of GSI's accelerator facility and the laser system nhelix, which is also described in this work.

The experiments focus on the measurement of the energy loss of medium heavy ions in a plasma created by directly heating a thin carbon foil with the nhelix laser, at an energy of about 50 J. In order to measure the energy loss using a time-of-flight method, a stop detector is used to register the arrival of the ion pulses after passing the plasma and a 12 m drift space.

At the beginning of the work on this thesis, the ion detector types formerly used were found to be inadequately suited to the difficult task; this was changed during this thesis. The ion detector has to be able to temporarily resolve ion pulses with a frequency of 108 MHz and a width (FWHM) of 3 ns at a very low current. It also has to withstand the X-ray burst from the plasma with a dead time shorter than the difference between the X-ray and the ion time of flight between the plasma and the detector. In order to satisfy these and other demands, a new diamond detector was designed and has now been used for several measurements. In addition to the new detector, other improvements were made concerning the diagnostics and the laser. The laser-created plasma now reaches a maximum temperature exceeding 200 eV and a free electron density of up to 10^{22} cm$^{-}3$.

With this greatly improved setup, energy loss data could be obtained with a temporal resolution several times better than before, using an ion beam with a diameter of only 500 μm. Additionally, thin foils of 0.5 μm thickness could be used, compared to 1.5 μm used before. These foils are very quickly turned into a fully ionized plasma by the laser pulse, so the resulting plasma is more homogeneous than with thicker foils. With the previous detectors, thicker foils had to be used due to the lower detector resolution.

The newly acquired energy loss data exhibits some unusual characteristics. At the beginning of the interaction of laser and plasma, the energy loss first decreases, then increases again, up to an energy loss 30% higher than the energy loss in the cold matter, then continues to decrease slowly. Several changes were made to study possible explanations for this behavior, including a change in the geometry of the setup to investigate whether fields could be responsible for the decrease.

Contents

List of Figures

Chapter 1

Introduction/Motivation

Energy loss of ions in matter has been a subject of research for the past decades. Energy loss in solid and gaseous targets is well known, but energy loss in partially or fully ionized matter, i.e., plasma, has been little understood so far. However, energy loss of ions in plasma is important in many applications, including heavy-ion driven hohlraum converter targets for inertial fusion [Sch07].

Members of the Laser and Plasma Physics group of Darmstadt University of Technology (TU Darmstadt) conducted experiments on energy loss in laser-produced plasmas during several experimental campaigns at the UNILAC accelerator of the Gesellschaft für Schwerionenforschung (GSI) in Darmstadt.

In these experiments, a laser plasma is created from a thin carbon foil by irradiation with a high-power laser pulse. An ion beam pulse from the UNILAC is then sent through this plasma and its energy loss is analyzed. Several diagnostic methods are used to investigate the ions, the plasma and the laser pulse.

Most theoretical descriptions of the energy loss of ions passing through ionized matter rely on a modified formula by Bethe, Bohr and Bloch (e.g. [Pet91]). The experiments performed at GSI provide new experimental input in order to improve this theoretical knowledge and to compare new simulations and theories with experimental data.

Chapter 2 gives a short overview of the theoretical background relevant to the experiments described in this work.

In chapter 3, the experimental setup of these experiments and their integration into the GSI accelerator system is described. An overview over the Z6 experimental area and the diagnostics used is given.

As measurements of ion energy loss with a newly developed ion detector are a key feature of this work, the techniques of ion detection, detector de-

velopment and results of measurements using this detector are discussed in detail in chapter 4. Another important diagnostic tool is an interferometry setup which makes it possible to obtain spatially resolved information about the free electron density in the plasma, an important parameter in energy loss measurements. Chapter 5 describes in detail the experiments performed within the frame of this thesis.

A final summary and discussion of the results presented in this work and an outlook on future possibilities are given in chapters 6 and 7.

Chapter 2

Theoretical Background

In this chapter, the theoretical background relevant to the experiments carried out within the scope of this thesis is provided. The study of the energy loss of ions in laser-produced plasma deals with a very complex subject and incorporates elements from several areas of physics, mainly laser physics, plasma physics, atomic physics, accelerator and charged particle beam physics, and the interconnections between them.

For any research involving laser-produced plasmas, knowledge of both plasma physics and laser physics is necessary. The mechanisms of plasma creation by high-power lasers have to be studied, focusing on the interaction of high-power lasers with solid matter and the formation of plasma. Plasma physics is important in order to understand the behavior of the plasma created. Also, the interaction between laser and plasma has to be investigated.

Finally, for the measurement of the energy loss of accelerated heavy ions in laser-produced plasmas, knowledge of accelerator and beam physics is required, including the interaction of beam ions with solid matter and plasma in general. The interaction between accelerated heavy ions and laser-produced plasma is the central topic of this work.

This chapter is split into three main parts: section 2.1 briefly explains some characteristic properties of plasma and introduces several key concepts of plasma physics. The following section 2.2 covers two laser plasma topics: first, the creation of plasmas using high-power lasers, and second, the interaction of high-power lasers with matter, especially with plasma. Section 2.3 discusses the mechanisms of energy loss of heavy ions in matter in general and in plasma in particular.

2.1 Plasma

2.1.1 Basic properties of plasma

Plasma is a state of matter roughly described as an ionized gas or conducting gas; however, it is usually much denser than an ordinary gas and its properties and behavior differ from that of a gas. A plasma is a mixture of ions, free electrons, and - depending on the degree of ionization - neutral atoms. The most important difference between a plasma and other states of matter is the presence of free electrons in a plasma.

There are several theoretical approaches to describe a plasma. A common approach is to treat the plasma as a mixture of electrons and ions, each with their own respective densities, temperatures and velocities. In this work, this approach to treat ions and electrons separately is also applied.

In order to characterize a plasma, several properties and parameters must be known. The following sections describe some key concepts about plasmas which are relevant to the understanding of this work.

Quasineutrality

In a plasma, the sum of the free electron charges always equals the negative of the total ions' charge. Therefore, it is 'quasineutral': to an outside observer, there is no net charge, since there are as many negative as positive charges in the plasma.

Local thermal equilibrium

A plasma temperature (electron and ion temperature) can only be defined if there is local thermal equilibrium (LTE) in the plasma. LTE means that dynamic properties of the particles in the plasma (e.g. electron and ion velocities, population partition among excited atom states, ionization state densities) follow Boltzmann distributions:

$$n_{jm} \propto exp{-\frac{\varepsilon_{jm}}{k_B T}} \tag{2.1}$$

Usually, LTE can be assumed in the plasmas that are the subject of research in this work. This is necessary, because otherwise it would not be possible to work with the concept of ion and electron temperatures in the plasma.

Debye screening and Debye length

The Coulomb potential for a charge q at a distance r is given by

$$\varphi_{coul}(r) = \frac{q}{4\pi\varepsilon_0 r} \tag{2.2}$$

In a plasma, this Coulomb potential is changed and weakened by the free electrons. These act as a shield, so that the Coulomb force has a finite range, as a positive ion becomes electrically 'invisible' behind a screen of free electrons. Within a certain range, there exists a modified coulomb potential called the Debye potential $\varphi_{debye}(r)$, but outside this range, the potential drops to almost zero because it is screened off by the electrons. This screening length is characteristic for a plasma and is called the Debye (screening) length λ_D.

$$\varphi_{debye}(r) = \frac{q}{4\pi\varepsilon_0 r} e^{\frac{-r}{\lambda_D}} \tag{2.3}$$

$$\lambda_D = \sqrt{\frac{\varepsilon_0 T_e}{n_0 e^2}} \tag{2.4}$$

For a detailed derivation of $\varphi_{debye}(r)$, see e.g. [Nis00].

Plasma frequency

If the free electrons in the plasma are displaced in respect to the ions, the space charge will lead to a restoring force. This force acts on the electrons; as the ion mass is much larger than the electron mass, the ions can safely be assumed to be stationary, while the electrons oscillate against the ion grid with a certain frequency called the electron plasma frequency ω_p:

$$\omega_p = \sqrt{\frac{n_e e^2}{\epsilon_0 m_e}} \tag{2.5}$$

Here, e is the electron charge, n_e the free electron density and m_e the electron mass.

In the present case of a non-relativistic plasma, where m_e is constant, the plasma frequency is a function of the electron density only. This plasma frequency is a very important quantity in the interaction of lasers with plasma, which is described in the following sections.

2.2 Laser-created plasmas

2.2.1 Creation of laser plasmas

There are several ways to create plasmas. Depending on the setup, gas discharge and z-pinch plasmas are mostly limited to a maximum density on the order of $10^{19}\,\mathrm{cm}^{-3}$ and temperatures of up to 40 eV [Hof94]; only exceptional z-pinches, e.g. the Z machine at Sandia National Laboratories, can reach temperatures in the keV regime [Jon09]. In order to create plasmas of higher densities and temperatures, thin foils are heated directly by a laser. This method is used in the experiments described in this thesis.

In this work, a plasma is produced by direct heating of a solid carbon foil target with a Nd:YAG laser. The nhelix laser used in this work has a wavelength of 1064 nm (Nd:YAG), so electron densities of $10^{21}\,\mathrm{cm}^{-3}$ and higher can be reached.

Laser plasmas incorporate two mechanisms of laser-matter interaction. First, the laser interacts with solid matter and creates a plasma. Then, the laser interacts with the newly created plasma for the remaining duration of the laser pulse.

If a solid target is hit by a high-intensity ($> 10^{10}\,\mathrm{W/cm}^2$) laser beam, a plasma is created on the surface of the target. This limit is dependent on the wavelength of the laser and the properties of the target material. The laser couples to existing free or weakly bound electrons within the target material which then start to oscillate within the laser electromagnetic field. More electrons are then freed through collisions, so the amount of free electrons increases very rapidly. A plasma forms on the surface of the target which expands at the speed of sound.

2.2.2 Laser-plasma interaction

The interaction between a high-power laser and a plasma is very complex, and the laser energy is transferred to the plasma by many different mechanisms, depending on various plasma and laser parameters such as plasma density and laser wavelength. Those mechanisms important to the experiments performed within the frame of this thesis are detailed here, along with several key concepts such as the critical density of the plasma.

Critical density

The laser can only propagate into the plasma up to a certain electron density. In vacuum, the laser light propagates as a transverse electromagnetic wave

with the dispersion relation

$$\omega_L^2 = k^2 c^2 \tag{2.6}$$

where ω_L is the laser frequency, k the wave number and c the speed of light. For an electromagnetic wave propagating through plasma, this dispersion relation is modified to include the plasma effects:

$$\omega_L^2 = k^2 c^2 + \omega_p^2 \tag{2.7}$$

If we solve for the wave number k, we find that it becomes imaginary if the laser frequency ω_L is below the electron plasma frequency (see eq. 2.5). This means that the wave cannot propagate in the medium, so the laser light can only propagate into the plasma up to this so-called critical density:

$$n_{e,crit} = \frac{m_e \varepsilon_0}{e^2} \omega_L^2 \tag{2.8}$$

The critical density is the electron density where the plasma frequency ω_p (which is itself a function of the free electron density) is equal to the incident laser frequency ω_L. In non-relativistic plasmas, this critical density $n_{e,crit}$ is dependent on the laser frequency ω_L only. For the nhelix laser, the critical density is $n_{e,crit} = 1.021 \cdot 10^{21}\,\mathrm{cm}^{-3}$.

Within the frame of this thesis, lasers are not only used to create the plasma, but also as a diagnostic tool for interferometric measurements which are explained in detail in section 5.4. The presence of a critical density means that the diagnostic laser cannot penetrate the areas of higher density than $n_{e,crit}$, so these are not experimentally accessible with this method. Note that the critical density is proportional to the square of the laser frequency, so if the laser frequency is increased, the critical density also becomes higher. Therefore, the interferometry laser used in these experiments is frequency-tripled.

Corona

Within a laser-created plasma, three main characteristic areas can be defined: the corona, the re-emission zone or energy transport zone, and a shock wave or compression area. This is illustrated schematically in fig. 2.1.

If a laser interacts with a laser-created plasma, there is a surface of critical density. In front of this surface, there is expanding plasma with undercritical density, so it can be penetrated (and heated) directly by the laser. This part is called the corona.

This corona has a high temperature and low density [Eli02].

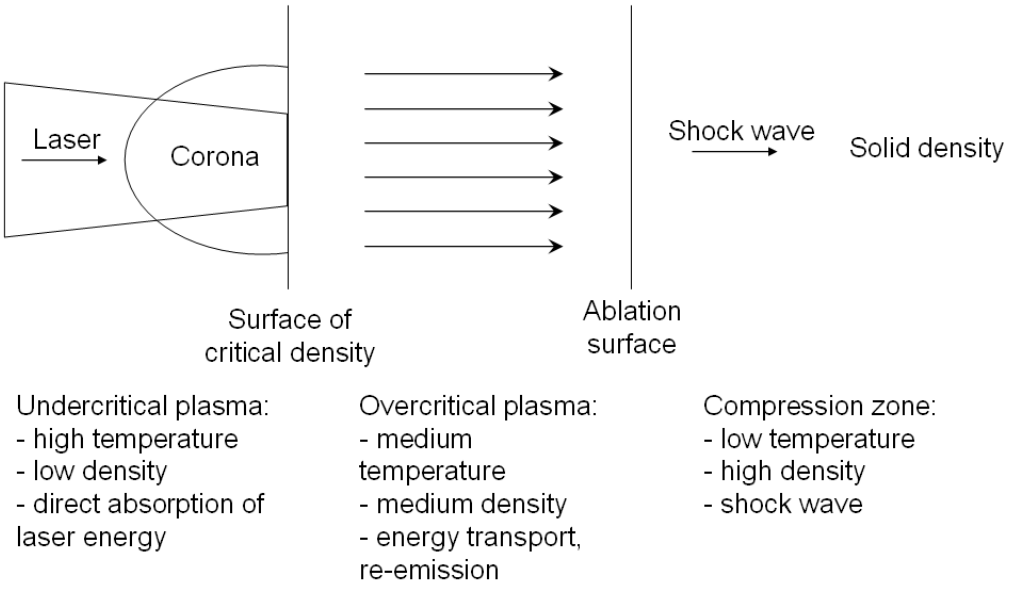

Figure 2.1: Schematic drawing of the inner structure of a laser-produced plasma. The three different zones (corona, re-emission zone/energy transport zone, compression zone) are separated by the surface of critical density between the undercritical corona and the overcritical plasma in the energy transport zone, and the ablation surface between energy transport zone and solid. In reality, of course, these boundaries are not fixed, but constantly moving.

The transfer of laser energy to the plasma in this area occurs mostly in the form of (collisional) absorption (see sect. 2.2.3). Also, collisions between electrons and ions are common, so x-rays are produced by interaction between photons and electrons. These x-rays are also used as a diagnostic tool in the experiments, which will be discussed in detail in chapter 4.

Energy transport or re-emission zone

Between the critical density surface and the ablation surface of the solid, there is a zone of overcritical plasma. This is an area of lower temperature, as the laser cannot heat this volume directly and energy is transported within the plasma. The density increases up to solid density, the temperature ranges between about 30 eV and 1000 eV [Eli02].

X-rays from the corona may enter this zone. The critical density, which is a function of the wavelength, is higher for them than for the laser light,

since they have a shorter wavelength than the laser light. These x-rays can be re-emitted, therefore this zone is also called re-emission zone.

Shock wave area

After this zone, behind the ablation surface, there is a shock wave area with density higher than solid state density. This shock wave propagates through the target, from the plasma side to the solid density side. In this zone, the shockwave-driven density can reach several times the solid density. The temperature varies; it is higher near the ablation surface and low within the solid.

In thin foil targets, which are used in the experiments described in this thesis, the shock wave and ablation surfaces travel through the entire target very quickly. As soon as they reach the back side of the foil, all solid matter will be transformed into plasma, which expands further and eventually becomes completely undercritical.

2.2.3 Transfer mechanisms of energy to plasma

There are several ways to transfer laser energy to the laser-generated plasma. It depends on the laser and plasma parameters which mechanism is the most common. In the experiment described in this work, the main transfer mechanisms of laser energy to plasma are collisional absorption (inverse bremsstrahlung) and resonant absorption.

Collisional absorption (inverse bremsstrahlung)

Collisional absorption is the absorption of energy from a photon into an electron during a collision. If an electron, e.g. from a high-energy electron beam, is fired at matter and decelerated and deflected by collisions with nuclei, it emits photons as bremsstrahlung. If high energy photons, as from a laser, are fired into matter, the opposite occurs: an electron absorbs a photon during a collision with an ion or another electron. The photon energy is thus transferred to the electron.

Langmuir waves (resonant absorption)

Langmuir waves are electron plasma waves. If the irradiating laser has an electromagnetic field component in the direction of the plasma density gradient, the laser can excite a longitudinal electron plasma wave known as Langmuir wave. At the layer of critical density (cf. eq. 2.8), there is a resonance and maximum absorption of laser energy, so the energy is converted

locally into kinetic oscillation energy of electrons. Only when this Langmuir wave is then dampened is this energy converted into heat energy.

With the resonant absorption mechanism, relatively few electrons receive a high amount of energy, whereas collisional absorption distributes a lower amount energy to many electrons.

2.2.4 Transport of energy within the plasma

There are three main mechanisms to transport radiation within a plasma. These are bound-bound transitions (line radiation, line absorption), bound-free transitions (radiation capture, photoelectric effect) and free-free transitions (bremsstrahlung, inverse bremsstrahlung).

2.3 Energy loss of ions in matter

2.3.1 Energy loss of ions in solid and gaseous targets

If accelerated ions pass through matter, they lose kinetic energy. The key quantity in describing this mechanism is the stopping power S, which is described by the differential energy loss $-dE_{proj}$ of a projectile ion per distance dx within the matter:

$$S = \frac{-dE_{proj}}{dx} \tag{2.9}$$

Since the projectile kinetic energy is, in the non-relativistic regime, dependent on the projectile velocity only, the stopping power S is then often written as a function of this velocity: $S = f(v_{proj})$.

Mainly, two processes cause the energy loss of a projectile passing through matter. These are collisions with nuclei and with electrons within the target matter. Collisions with nuclei are elastic collisions caused by the projectile's interaction with the Coulomb potential of the nuclei. Collisions with electrons are inelastic collisions, where ionization processes between target matter and projectile occur.

The stopping power S can thus be regarded as the sum of the individual stopping powers caused by target nuclei and target electrons:

$$S = S_{nucl} + S_{electr} \tag{2.10}$$

One approach to the situation is to examine a moving ion on a straight trajectory along the z axis, passing a target particle at rest at a minimum

distance of b in the x direction. For the electric Coulomb field of the ion, $\vec{E}(t)$, the transfer of momentum is

$$\Delta p = e \int_{-\infty}^{\infty} \vec{E}(t) dt \tag{2.11}$$

The trajectory of the ion is represented by

$$\vec{r_i} = v_i t \vec{e_z} + b \vec{e_x} \tag{2.12}$$

The electric field can be written as

$$\vec{E}(t) = e Z_{proj} \frac{(\vec{r})(t)}{r(t)^3} \tag{2.13}$$

So, the change in energy is:

$$\Delta E = \frac{(\Delta p)^2}{2 m_T} = \frac{2 Z^2 e^4}{m_T v_i^2 b^2} \tag{2.14}$$

for an ion represented by a point charge with $\frac{1}{r^2}$ potential, charge state Z and velocity v, passing a particle of mass m_T at rest. This shows that the energy loss of the ion rises proportionally to the square of the ion's charge-to-velocity ratio, and that the energy loss is inversely proportional to the mass of the target particle. Thus, ions lose more energy through collisions with target electrons than with the target ions.

In order to be able to actually calculate the stopping power, the sum of all possible ΔE has to be taken, and minimum and maximum values of b have to be stated, otherwise the resulting integral diverges. If this is done (for details see, e.g., [Fra08]), the result is a well known formula originally published by Bethe [Bet30]:

$$S(x) \approx \frac{4\pi Z_{proj}^2 Z_{target} e^4}{m_e v_{proj}^2} n_{target} \ln \frac{2 m_e v_{proj}^2}{I_0} \tag{2.15}$$

Here, n_{target} is the particle number density of the target and I_0 the mean ionization potential of the target.

The mechanisms of energy loss in solid and gaseous targets are well known, and very accurate predictions can be made using e.g. codes like SRIM (Stopping and Range of Ions in Matter, [Zie03]). The energy of the ions is transferred to the target mostly by collisions with the target electrons. Other effects (photoelectric effect etc.) play a role depending on the projectile charge state and the projectile energy. For projectile energies below 100 keV/u, collisions with target nuclei must be taken into account. For projectile energies above 1 MeV/u, energy loss to the target electrons is the dominating effect, so $S_{nucl} \ll S_{electr}$, as can be seen in fig. 2.2.

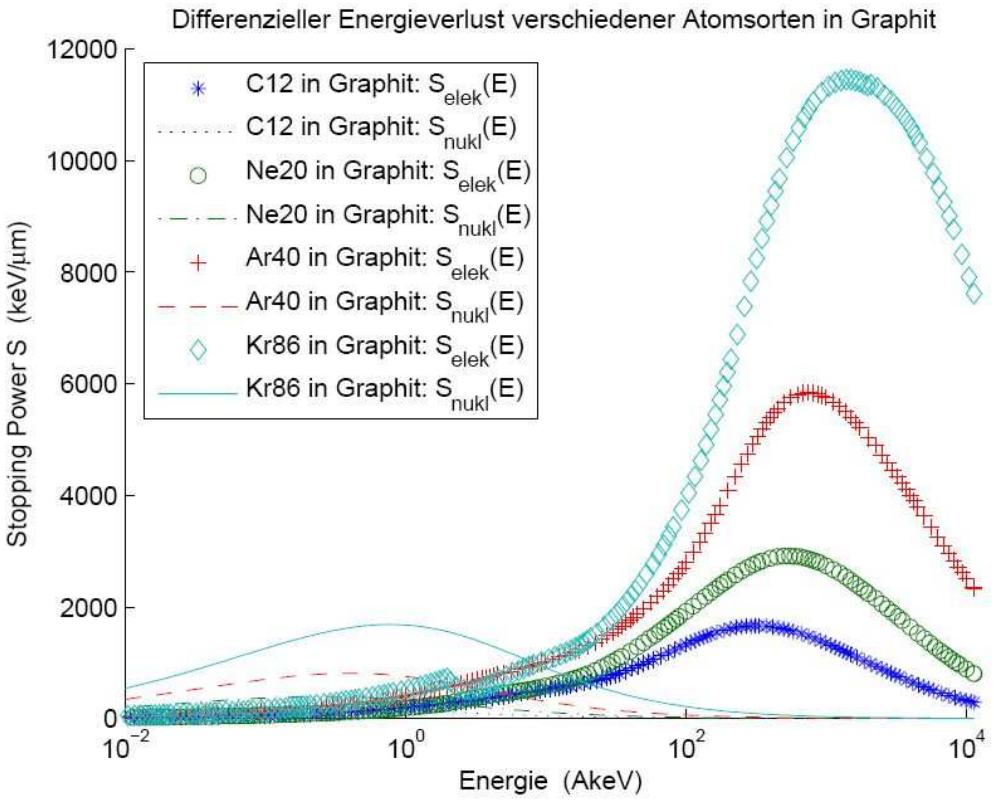

Figure 2.2: SRIM 2003 calculations (from [Wam06]) showing the ratio between energy loss to nucleons and energy loss to electrons for four different projectile ion species in graphite. The energy loss to nucleons is shown as lines, the energy loss to electrons as symbols only. As expected, he energy loss is generally higher with higher Z of the projectile ions. The graphs clearly show that for low energies, the energy loss to target nucleons exceeds the energy loss to target electrons, but at higher energies, above 100AkeV, the energy loss to target electrons by far dominates the energy loss to nucleons in every case.

2.3.2 Effective charge state and equilibrium charge state

The projectile ions used in the experiments described in this work enter the plasma in a known charge state. However, there are several processes which change a projectile's charge state during the propagation through a target.

In a solid target, the charge state will increase mainly by coulomb collisions with target ions, but decrease due to recombination by the capture of bound electrons within the target. There are other effects, but these two are the dominant mechanisms. The recombination and ionization rates can be calculated using the ratio between cross sections for these processes. This 'equilibrium' charge state is reached after a short time of flight through the target matter. For heavy ions, the equilibrium charge state can be calculated using semi-empirical formulas [Bet83]. These formulas also work well with gaseous targets.

The effective charge state, however, is not the real charge state, but an artificial construction used in most older calculations.

2.3.3 Energy loss of ions in plasma

Energy loss of ion projectiles in a plasma differs from that in solid targets due to the properties of plasma, especially the free electron density. Energy can be transferred to free electrons in a plasma.

2.3.4 The modified Bethe-Bloch-Bohr formula

Most of the concepts of energy loss of ions in matter are based on theoretical works of Bethe, Bohr, and Bloch ([Bet30],[Blo33],[Boh13]). The original Bethe formula 2.15 was modified using the idea that energy loss in plasma would be the same as energy loss in a solid target, but with an additional term due to the contribution of free electrons. So, the formula contains two energy loss terms, one relating to bound electrons (as in a solid target), the other to free electrons.

$$-\frac{dE}{dz} = \frac{16\pi a_0^2 I_H^2 Z_p^2}{m_e v^2}\left[\sum_{Z=0}^{Z_k}(Z_k - Z)n_z \ln\frac{2m_e v^2}{I_z} + n_e \ln\frac{2m_e v^2}{\hbar\omega_p}\right] \qquad (2.16)$$

Here, Z_p is the charge state of the projectile ion, n_z the density of ions of charge state Z with atomic number Z_k; n_e is the free electron density. In the free electron term, $\hbar\omega_p$ signifies the plasmon energy, the amount of energy that can be transferred by collisions to the free electrons of a plasma.

Since the energy loss is dependent on the square of the charge state, energy loss in a plasma with a lower recombination rate and thus generally higher charge state is higher than in a solid target, according to this theory.

2.3.5 Mechanisms of projectile charge state change

If a projectile passes through matter, charge state changes can occur either via electron loss or electron capture.

A projectile may lose electrons through collisions with ions (CII, Collisional Ionization by Ions) or collision with electrons within the target (CIE, Collisional Ionization by Electrons).

Electron capture occurs through one of the following processes: Bound Electron Capture (BEC), Radiative Electron Capture (REC), Dielectronic Recombination (DR) and Three-Body Recombination (3B).

A detailed overview of these processes can be found in [Jac98]

Chapter 3

Setup of the Z6 experimental facility

In this chapter, a summary of the setup for the experiments performed at the Z6 area within the scope of this work is given. The Z6 experimental facility at GSI uses the combined possibilities of the UNILAC (UNIversal Linear ACcelerator) accelerator and the nhelix laser system. The nhelix system provides both the plasma-creating laser beam and a diagnostic laser beam while the UNILAC delivers the ions whose energy loss in the plasma is the subject of this work.

In section 3.1, the UNILAC accelerator is described, and technical aspects important to the experimental work at Z6 are presented. In particular, details about the bunch structure of the UNILAC are explained, as these are crucial to the energy loss measurements of the beam ions.

In the following section 3.2, an overview of the nhelix laser system is given and the different laser beams are detailed.

After that, in section 3.3, the setup of the experiments at the Z6 experimental facility is described, with a focus on the target area, where laser beams, target, plasma, and ion beam interact.

Many types of diagnostics are needed to perform energy loss measurements of heavy ions in laser-produced plasma. In the last section of this chapter, section 3.4, an overview of these is given.

3.1 The UNILAC accelerator

The UNILAC can accelerate any ion species up to uranium. It provides ion pulses of different ion species with an energy of 3.6 MeV/u to about 18 MeV/u.

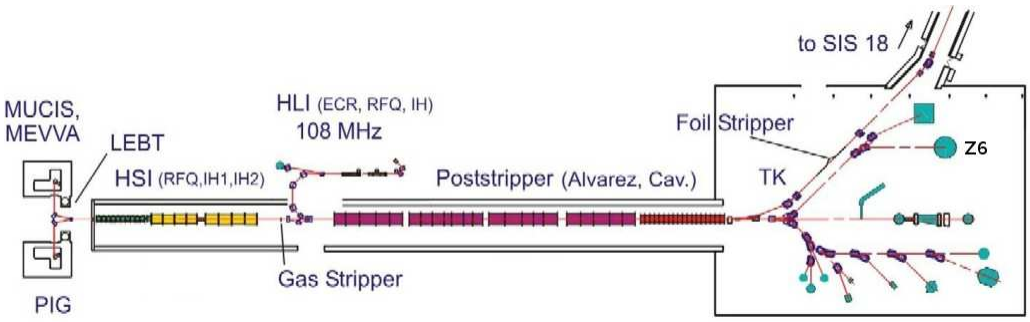

Figure 3.1: Location of the Z6 experimental area within the UNILAC accelerator facility (image (c)GSI)

There are three different ion sources available, which are shown in figure 3.1. The two ion sources at the left of the image, called injectors North and South, provide ions with low charge states. These ions are accelerated from the ion source through an RFQ (Radio Frequency Quadrupole) section, which operates at a frequency of 36.136 MHz. This frequency is imprinted on the ion beam bunch structure of the ions originating from injectors north and south and corresponds to a peak-to-peak distance of 27 ns. The ions can afterwards be stripped in a gas stripper in order to reach a higher charge state before they reach the Alvarez section, where they are accelerated further. An Alvarez structure is a type of linear accelerator element where a series of drift tubes is arranged in a copper tank. A cavity wave is induced directly into this structure. The UNILAC Alvarez section consists of four tanks and operates at a frequency of 108.41 MHz. However, not each of these HF pulses is used with the injectors North and South, since they operate at a frequency of 1/3 of the Alvarez frequency. Here, only every third Alvarez cavity is filled with ions.

The third ion source, HLI (HochLadungsInjektor, High Charge State Injector), is located to the north of the accelerator complex, between the RFQ and the Alvarez sections. This injector is designed to produce ions with a high charge state and uses an ECR (Electron Cyclotron Resonance) ion source. The ions from the HLI are, after a first accelerator stage, directly injected into the Alvarez section and use the full Alvarez frequency, corresponding to a peak-to-peak distance between pulses of only about 9 ns.

The maximum energy of the ions after the four Alvarez tanks is 11.4 MeV/u. However, behind the Alvarez section there is a single resonator section, which accelerates the ions to higher energies, depending on the ion species. Maximum energies of the single resonators for $^{130}Xe^{21+}$, $^{238}U^{28+}$ and $^{20}Ne^{7+}$ are 14.3 MeV/u, 13.5 MeV/u, and 17.7 MeV/u, respectively [GSI09].

The details of the bunch structure are described in the following section.

3.1.1 The ion beam bunch structure

The ion beam has a twofold bunch structure imprinted on it by the accelerator. A so-called macro bunch is a millisecond (can be adjusted from 0.5 ms to 5 ms) pulse with 20 ms between pulses. This macro pulse frequency is forced by the 50 Hz frequency of the power network. Each macro bunch consists of micro bunches. This micro bunch structure is determined by the accelerator frequency and the ion source. If the accelerator is running the North and South ion sources, due to the built-in frequency of the RFQ the distance between the micro bunches is about 27 ns. This is a temporal resolution problem for the measurements done in this work, since most plasma effects take place within the first 10-30 ns of the plasma ignition.

The ions from the HLI ion source do not pass through the main RFQ section, but are injected through their own RFQ structure directly into the Alvarez section which runs at 108 MHz. So, for HLI ion beams, the micro bunches have a FWHM width of 2-3 ns and a peak-to-peak distance of 9.2 ns, corresponding to the 108 MHz Alvarez frequency. Figure 3.2 is a schematic drawing of these micro pulses.

A single bunch temporal profile approximately follows a $\cos^2$ function. However, to facilitate calculations, we assume it to be Gaussian-shaped. Since we are interested mostly in the location of the peaks, the exact form of the curve is irrelevant as long as the central peak remains. Also, a $\cos^2$ curve and a Gaussian curve are shaped very similarly.

3.2 The nhelix laser system

The name nhelix is an acronym for "Nanosecond High Energy Laser for Ion eXperiments". Figure 3.3 shows an overview of the entire system. The nhelix laser system consists of up to three laser beams driven by independent Nd:YAG oscillators, marked OS1 and OS2. In the experiments described in this work, two beams are used, one from OS1 for plasma heating and one from OS2 for interferometry diagnostics. The main beam of OS2 is not used.

Beam 1, the beam used for heating the target and thus generating the plasma, is driven by oscillator OS1 (model Powerlite Precision 8000, Continuum). Beam 2 is used as a diagnostic laser in the energy loss experiments and is driven by oscillator OS2 (model G-Mini-B100-GSI, Geola Technologies).

The beam created in OS1 is amplified in a series of Nd:YAG and Nd:glass amplifiers. The wavelength of the beam is 1064 nm (Nd:YAG). Before and

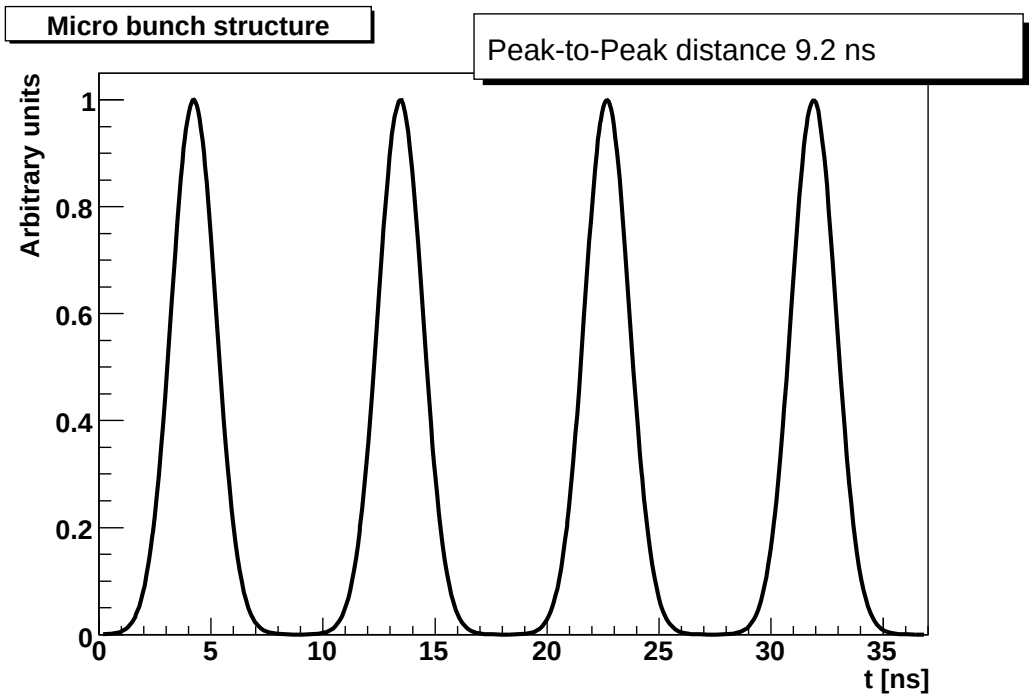

Figure 3.2: Schematic representation of the micro bunch structure of the UNILAC accelerator using the HLI injector

in between the amplifiers, the beam diameter is increased in order to remain below the destruction threshold of the optical components as the beam energy increases. Kepler telescopes are used to increase the beam diameter, and in the focal plane of these telescopes, apertures are used to filter out high spatial frequencies, so this setup acts also as a spatial filter which smoothes the beam profile. The amplifiers work with beam diameters of at first 16 mm, then 25 mm, 32 mm, 45 mm and, in the last stage, 64 mm.

Oscillator 1 uses a Pockels cell as an active Q-switch and creates a Gaussian-shaped pulse with a pulse length of 15 ns (FWHM). However, for the purpose of creating a plasma, the laser pulse shape should have a sharply rising edge in order to heat the foil target instantaneously. Another Pockels cell is used to transform the Gaussian shape into an almost rectangular shape, to obtain this sharply rising edge. The rate of rise of the pulse is limited by the time the Pockels cell needs to apply the voltage; the rise time is 3 ns.

After passing the entire amplifier chain, beam 1 delivers up to 100 J in a 10 ns (FWHM) pulse. In the experiments described in this work, a shorter pulse (5 ns FWHM) with an energy of 50 J was used. In the most recent beamtimes, a random phase plate was inserted into beam 1 before the laser

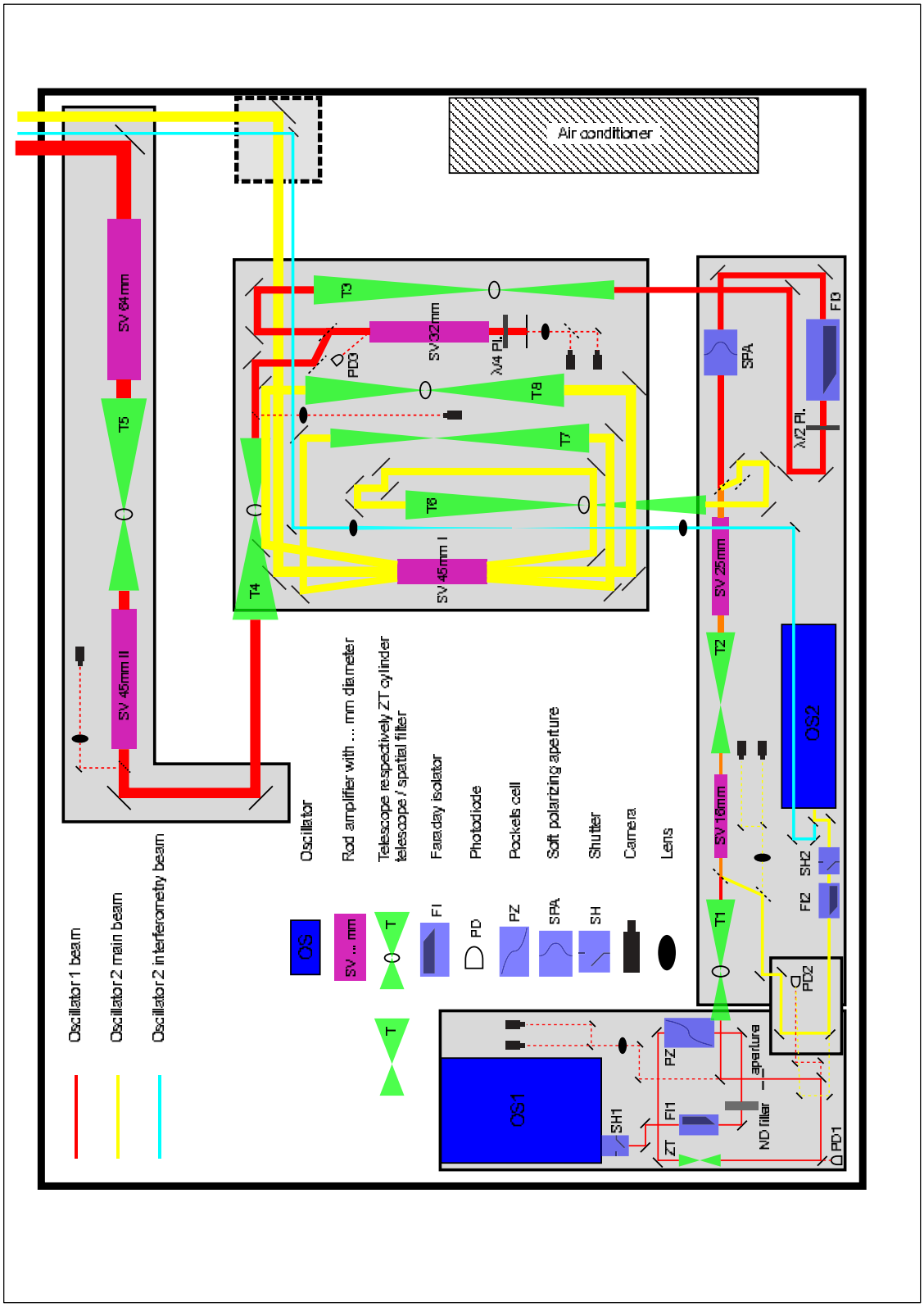

Figure 3.3: Schematic drawing of the nhelix laser system

beam reaches the foil target, to create a homogeneous flat-top laser pulse shape. This phase plate is located after the final focusing lens, cf. figure 3.4. It was added to the setup at the beginning of 2007, so it is not present in the first measurements made within the temporal frame of this thesis.

The pulse of beam 2 is also created in a Nd:YAG oscillator with an active Q-switch; it has a FWHM of 5 ns which is then shortened to 0.5 ns using an SBS (Stimulated Brillouin Scattering) box [Men01]. Since this laser beam is only needed for interferometry purposes in the energy loss experiments described in this work, it is not used at full energy. It does not pass through the amplifier chain but is extracted directly after the oscillator OS2, as is shown in fig. 3.3.

The wavelength is important for the use as an interferometry laser. Beam 2 can be frequency-doubled to a wavelength of 532 nm, which is in the visible range (green). It is also possible to triple the frequency of beam 2. At 3 ω, this beam has a wavelength of 355 nm. This is used for the interferometry measurements described in this work.

3.3 Setup of the energy loss measurement experiments

For the energy loss measurements, both laser beams and the ion beam have to be synchronized onto the target area, along with several diagnostic instruments, to the order of $\Delta t < 1$ ns.

Figure 3.4 shows the interaction of the ion beam and the laser beams 1 (heating laser) and 2 (interferometry laser) at the target area. The ion beam from the UNILAC is directed through a circular aperture whose diameter can be chosen between 1 mm and 300 μm, in order to overlap the ion beam and the laser area on the target in as small an area as possible. The laser is not adjusted for best focus on the target, but is always chosen to be larger than the ion beam spot. This is to ensure that the ion beam passes through a plasma with a homogeneous line density, not through the fringes of the laser plasma. The beam spot size has been tested using an RCF (RadioChromic Film) target.

3.3.1 The target chamber

Figure 3.5 shows a technical drawing of the Z6 target chamber. This target chamber is roughly spherical with 1 m in diameter. The ion beam axis is shown in yellow, the interferometry laser in green and the heating laser in red.

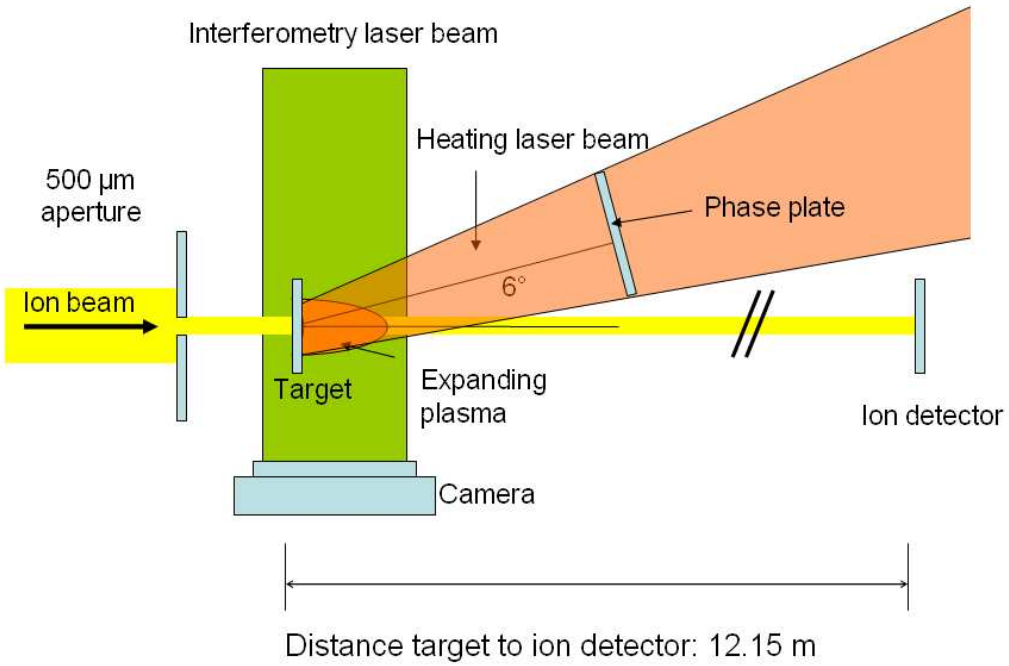

Figure 3.4: Schematic drawing of the energy loss experiment setup at the Z6 area

In the outer wall, as many windows (portholes) as possible are integrated, so there is enough space for cameras and other diagnostics to view the target area. The image shows 8 of the portholes used mainly as windows for various diagnostic devices. In addition to these, there are portholes at a 45 degree angle to the vertical, which are used e.g. as windows for the target positioning control camera. One of them is used as the entry window for the interferometry laser. This laser has to be able to cross the entire target chamber and the target without being obstructed by anything else than the plasma.

During a measurement, the red laser beam ignites the target, while the green laser beam passes through the plasma exactly at a 90 degree angle, which is essential for the interferometry method, as this method assumes cylindrical symmetry.

The target foil is mounted on an aluminum 'ladder' which accommodates several targets and can be adjusted automatically using a 3D motion controller (Newport Motion Controller Model MM4005), so the chamber does not have to be opened and re-evacuated after every measurement. Several measurements can be made using the same target ladder. The foil itself is

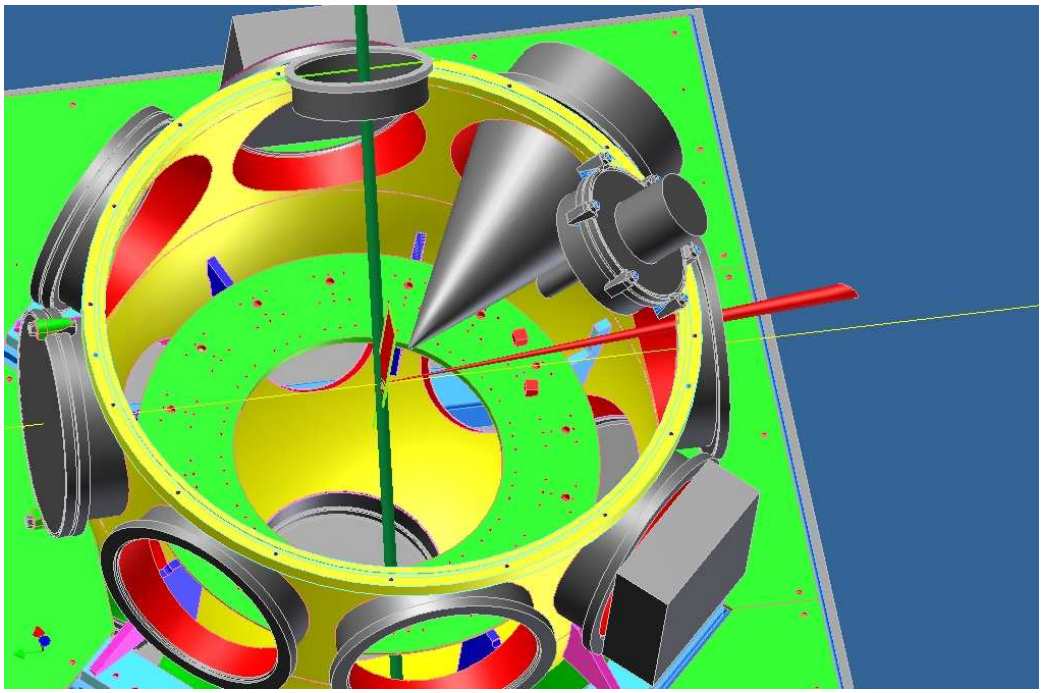

Figure 3.5: SolidWorks drawing of the target chamber [Zil08]

attached onto a small aluminum frame which allows the diagnostic laser to pass the foil without anything obstructing the laser path. However, different target holders are used for different target types.

The entire interferometry setup is located beneath this target chamber. The large cone within the target chamber in figure 3.5 is the tube for a pinhole camera.

When a CCD camera was used, this was set up to view the plasma from one of the side windows, so as to get a 90 degree image of the expanding plasma, in order to calculate the expansion velocity from that.

Around the target ladder, there is a fixed steel ring where lenses and other devices needed within the chamber can be securely mounted.

Before the laser pulse arrives at the target, the ion beam pulses are sent continuously through the target foil. Due to the relatively low energy deposition of the ions and the thinness of the foil, the foil is not damaged by this. When laser 1 hits the target, a plasma is created from the foil; the ion beam pulses thus propagate no longer through a solid foil, but through the plasma. At the same time, laser 2 penetrates the plasma at a right angle to the ion beam axis, and an interferometric image of the plasma is recorded by a camera. The interferometry setup and additional diagnostics are described

in detail in the following section.

3.4 Diagnostics

Three main types of diagnostics are used in these energy-loss experiment. Laser diagnostics have to be used for the heating laser beam and the interferometry laser beam, plasma diagnostics for the laser-generated plasma, and ion diagnostics for the heavy ion beam.

3.4.1 Ion beam diagnostics and alignment

Most key parameters of the ion beam, such as initial particle energy, charge state and beam current, are measured by the UNILAC diagnostics systems. The Z6 beamline is equipped with several quadrupole doublets. One of them is located in front of the target chamber; this is used to focus the beam onto the target inside the target chamber. Another two behind the target chamber is used to parallelize the now diverging beam.

Beam position

Two scintillators can be inserted by remote control into the beamline, one within the target chamber and the second right in front of the ion detector. They are observed by cameras. With these scintillators, the position of the beam can be checked quickly. They are also used for the first coarse adjustments of the beam when the beamline is taken into operation at the beginning of a beamtime.

For a finer adjustment of the beam position, 2D beam position grids are used. These are located in diagnostic boxes spread along the length of the beamline. One is situated in front of the target chamber, and two between the target chamber and the stop detector.

Beam current

The beam current can be measured at several positions within the beamline with Faraday cups and beam transformers. However, Faraday cups are destructive methods of beam current measurement. They are used to obtain current data between experiments. As a non-destructive measurement method to monitor the beam current during experiments, phase probes were used at two to three different locations along the Z6 beamline. These were equipped with extra amplifiers to boost their signal. Phase probes do not measure the beam current directly, so the destructive beam measurements

are necessary to obtain absolute information on the actual beam current. The probes measure the change in current, which is the derivative of the beam current with respect to time. Thus, the signals for the approximately Gaussian-shaped UNILAC micro bunches show a zero-crossing at the maximum of the bunch.

3.4.2 Laser diagnostics

Transverse beam profile and energy

To measure the transverse laser profile, a CCD camera was used (Cohu). A laser beam is sent directly through ND (neutral density) filters onto the very sensitive CCD, so an exact image of the transverse intensity profile can be taken. However, this cannot be done during the experiments, as it is also a destructive measurement. A calorimeter was used to record the laser energy on-line in each measurement, using a coupled-out small part of the beam.

A photo diode is used to measure the laser timing and longitudinal beam profile directly. The diode is time calibrated before the measurements by inserting a second diode into the place of the target, shooting the laser and measuring the time delay between the two diodes. Thus, in each measurement it can be determined at what time the laser hits the target.

3.4.3 Plasma diagnostics

A fast-shutter CCD camera (model PCO DiCam Pro) was used to observe the plasma in the visual range. These cameras have a minimum exposure time of 5 ns, so the images are integrated over the time of 5 ns. It is possible to estimate the expansion velocity from images taken at different times during the expansion; however, only one image could be taken in each measurement, so images taken at different times and in different measurements have to be compared.

An interferometer was used to examine the plasma during the measurement and to gain information on the electron density within the plasma. Initially, the interferometer could only take one image of the expanding plasma, but with the development of the multi-frame interferometry, it is planned to take more images.

The pinhole cameras can provide a view of the entire expanding plasma in the visual/X-ray range. A streak camera is used to make time-resolved images of a small area, using a slit. The Z6 group has two streak cameras, one operating in the x-ray range, one in the visible range.

Chapter 4

Energy Loss Measurement

4.1 The principle of energy loss measurement using TOF measurements

Accelerated ions passing through matter lose kinetic energy, as was explained in section 2.3. In order to measure the energy loss of ions in plasma quantitatively, the difference in ion energy before and after passing the plasma has to be determined. However, the absolute final energies are not important, only relative values are needed, as the initial energy of the particles in the UNILAC accelerator is known exactly.

The general idea behind the Z6 energy loss measurements is to use a TOF (Time-of-Flight) measurement rather than an energy measurement in order to determine the energy loss of the ions. Kinetic energy is, in the non-relativistic regime as is the case here, directly related to the particle velocity, and therefore, to the flight time over a given distance. An ion passing through matter will be slowed down and arrive at the detector after a longer flight time compared to an undisturbed ion, over the same distance, as is illustrated schematically in fig. 4.1. This delay is caused by energy loss in the target matter, and thus precisely the quantity of interest here.

A normal TOF measurement uses two detectors, a start detector and a stop detector, to determine the time of flight between two specific points. The TOF measurements used in this work employ a different method. Basically, only a stop detector is used, as we only need relative flight times. The details of this method are laid out in the following sections.

In each measurement, the ion beam is sent first through the still solid foil. Then the laser pulse hits the foil, and the beam passes through the plasma and gas cloud created by the laser, until, at the end of each measurement, the gas becomes so thin that the beam propagates through near vacuum. So,

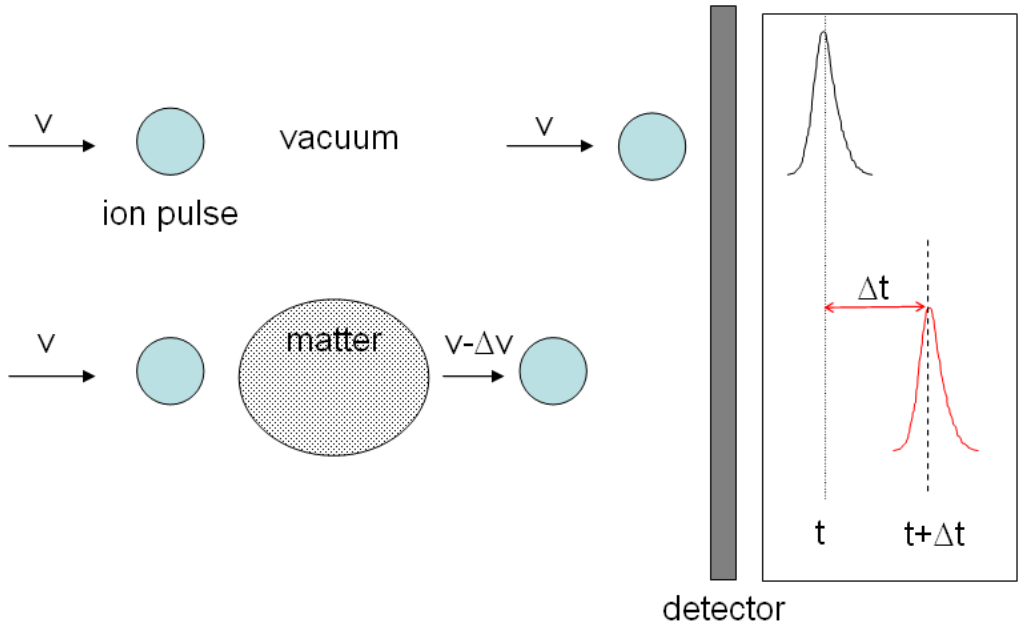

Figure 4.1: Schematic drawing of the underlying idea behind the TOF measurement used in this work. The ion bunch that has passed matter will decrease its velocity, since it has lost kinetic energy in the matter. The time delay Δt between the arrival of an undisturbed bunch (top) and the bunch that has experienced energy loss (bottom) is a measure of the stopping power.

there are four main stages in each measurement: a solid foil stage, a plasma stage, a gas stage and a vacuum stage.

Solid foil stage

If a target foil is inserted into the beam, the beam ions propagate through the thin foil and lose some of their energy in the solid target. This energy loss is always constant as long as the beam parameters remain unchanged, as the foil's thickness and density do not change when the beam passes through it. The intensity of the beam ions is too low to cause significant changes to the foil. Since the target material and charge state, mass and energy of the ions are known, the energy loss can not only be measured, but also calculated using e.g. the SRIM (Stopping and Range of Ions in Matter) code [Zie03]. These calculations match the experimental results obtained during all beamtimes. If the energy loss of the ions of each bunch is plotted over time, there is a plateau of constant value corresponding to the energy loss in

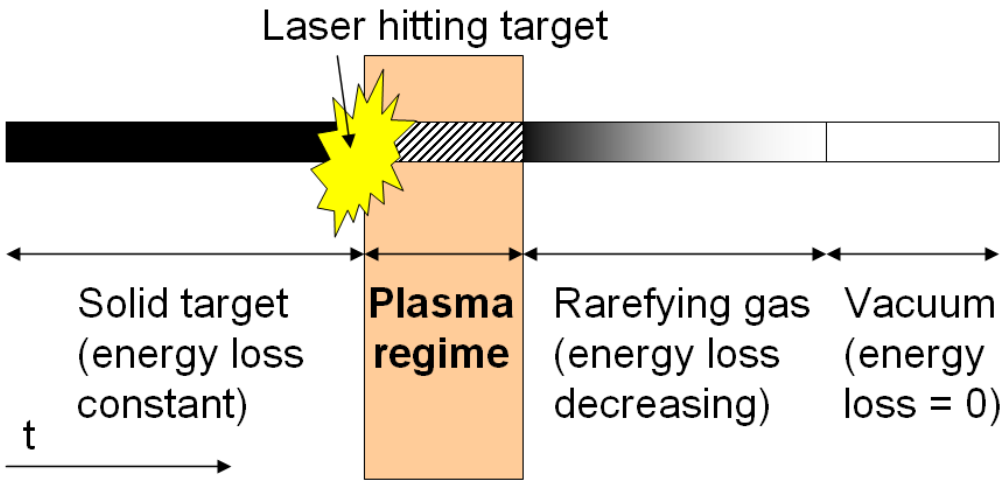

Figure 4.2: The four main stages of an energy loss measurement. At first, the ions pass through a cold foil, the energy loss is constant. Then the laser pulse starts to heat the target and turn it into a plasma; this most interesting region is called the plasma regime here. Later, the plasma starts to cool and dissipate, becoming thinner. In this stage, the energy loss decreases with time. The last stage, when the plasma has become so diluted that it can be considered vacuum, would show an energy loss of zero in theory. However, in the experiments, the energy loss would not drop to zero within the temporal frame of most measurements, as there was still residual rarefying plasma left within the target chamber.

the solid target. From this data, the exact foil thickness is then calculated.

Plasma stage

When the laser hits the target foil, a plasma is created. The thin foil is vaporized into an expanding plasma cloud. X-rays are emitted by the plasma, as described in section 2.2. The stop detector is not only able to detect ions, but it is also sensitive to x-rays. These x-rays are both advantageous and disadvantageous to the measurement. On one hand, the steeply rising flank of the x-ray signal is an exact marker for the time the plasma is created. On the other hand, the x-ray signal is so intense that the stop detector is temporarily "blinded" by it; it becomes saturated for several tens of nanoseconds and is, during that time, not able to detect the ion signals.

However, this problem is alleviated by taking advantage of the difference in flight time between the ions and the x-rays. The stop detector is placed at

a distance of 12.15 m to the target. As the x-rays from the plasma are only produced during the laser pulse length, this distance and the difference in velocity between the X-rays and the ions is enough to ensure that the detector can respond correctly again when the ion bunches that have traveled through the plasma arrive at the detector. Additionally, the X-Ray flash can be used to establish the correct timing, see section 4.1.2.

This plasma stage is the most interesting stage of the measurements, but also the stage which is most difficult to access diagnostically. Changes in the plasma take place on a nanosecond time scale.

Transition stage

In this stage, the plasma dissipates, cools and becomes more and more diluted, until near vacuum conditions are reached again within the target chamber.

Vacuum stage

When the ion beam propagates through vacuum, there is no energy loss; this "undisturbed beam" was used as a calibration in older measurements. In a measurement using a target, near vacuum conditions are reached at the end, where the gas from the vaporization of the target foil is very diluted and has expanded away from the ion beam axis.

4.1.1 Establishing a reference

In order to determine the energy loss of the ions, mainly the ion detector data is used. In the older measurements, a reference was established using the data from the vacuum stage. During that stage, the ions pass the entire distance between the target and the detector undisturbed, so the data from this stage is used as a reference. It establishes where the ion beam bunch signals for an undisturbed beam should be. The frequency, i.e. the distance from peak to peak, is constant and due to the frequency of the accelerator and ion source (see section 3.1). From the vacuum stage, it is calculated backwards in time to see at what times undisturbed ion beam bunches would arrive at the detector. The reference timing is established by taking many ion beam bunch signals from the vacuum stage, then taking the average of these and using this average to extrapolate for all earlier times. Then, the energy loss in the cold foil can be calculated, as the ion beam bunch signals in the solid foil stage have a constant temporal delay in comparison to the extrapolated peaks from the vacuum stage. This constant delay is due to the energy loss

in the cold target foil. The result is verified against SRIM [Zie03] data. It was found to be in good agreement, which is an additional cross-check for the energy loss measurement method used. However, this method of establishing a reference has the disadvantage that the diluted plasma reaches only near vacuum conditions, not exactly a vacuum, so the accuracy is limited. A more exact method has been employed during recent beamtimes, where the 108 MHz frequency of the accelerator was used.

4.1.2 Timing

In order to be able to compare data, the timing, i.e. especially the delay between laser pulse and ion beam micro bunch, has to be established for each measurement. The exact temporal relation between the laser igniting the plasma and the ion beam micro bunches is very important.

The laser pulse cannot be directly observed with the stop detector used for the ions, but it can be detected indirectly. When the laser starts to heat the target, x-rays are emitted immediately (cf. section 2.2.2). The detector is sensitive to these x-rays. For the 12.15 m flight distance between target and stop detector, x-rays have a flight time of 40.5 ns. The flight time of the argon ions is determined using the kinetic energy and the mass of the beam ions. Argon ions (16+) with a kinetic energy of 4.001 MeV/u have a velocity of 27599274,85 m/s. This corresponds to a flight time of 4,402e-7 s or 440,2 ns. The difference in flight time between the x-rays and the ions is thus 400 ns.

In the first experiments described in this work, only this x-ray method was used. In the most recent experiments, additionally a photo diode was used to observe the laser directly. This is described in section 3.4.2. The results of these two methods also were in good agreement. The photo diode method is more exact, as it measures the laser pulse without having to resort to secondary photons from the plasma, eliminating another source of error. The diode also yields detailed information on the temporal laser pulse shape, which the x-ray signal does not.

It is necessary to measure the laser impact time, instead of simply using the timing set on the laser control instruments, which are synchronized with the accelerator. The technical details of the synchronization between laser and ion beam can be found in [Fra08]. The delay generators used have some internal jitter due to technical limitations. Thus, the direct measurement is the most precise possibility.

Using the established laser hit timing as a time base, the reference is established. Ion micro bunch signals are expected to arrive every 9.2 ns according to the frequency of the UNILAC and the ion source used. Dur-

ing the solid foil stage, all ion beam bunches arrive with a constant delay corresponding to the energy loss in the foil.

Additional energy loss must result in an additional delay of the ion bunch signal, more than the delay expected because of the energy loss in the solid foil. This is pictured in figure 4.3, which shows the expected detector signals for the vacuum stage, the solid foil stage, and the plasma stage. The gas stage is not pictured, since it is only a transitory stage between the plasma and vacuum stages, with delays approaching zero as the plasma dilutes into near vacuum conditions.

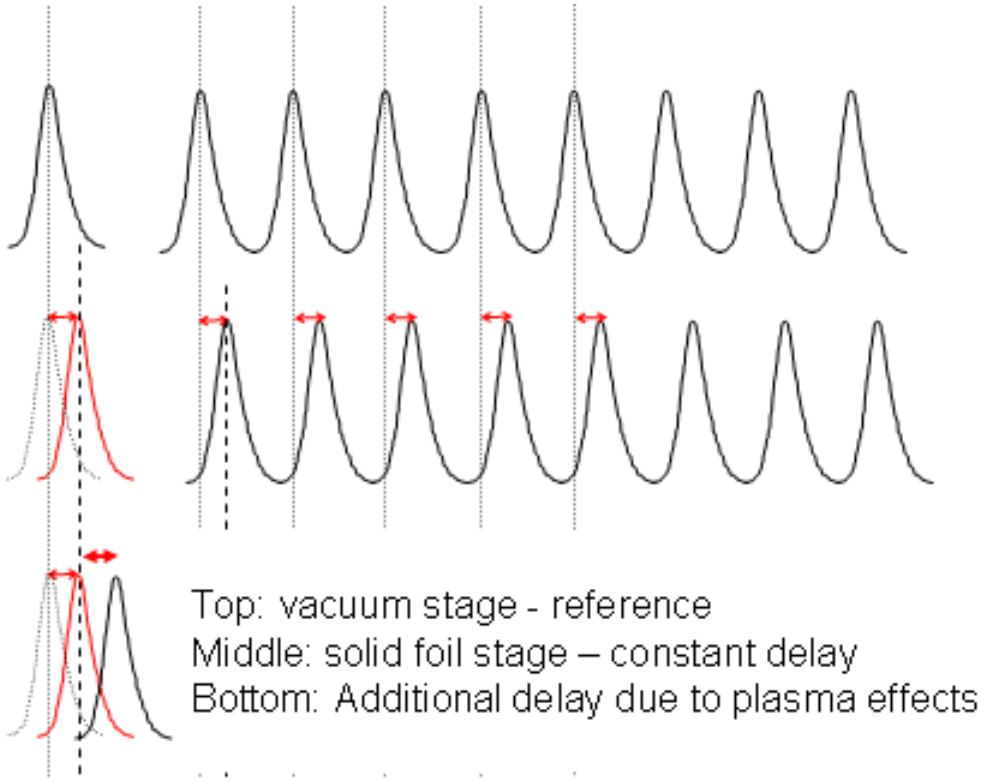

Figure 4.3: Schematic of the principle of ion detector data analysis. In the top part, the reference is shown, extrapolated backwards from the vacuum stage. Against this reference, in the middle part, the signals of ion bunches passing the solid foil are shown. These have a constant delay corresponding to the energy loss in the foil. In the bottom part, during the plasma stage any additional delay must be due to plasma effects.

4.2 Ion detector development and improvement of the experimental setup

The most important diagnostic tool in the energy loss measurements is the ion detector, since ion energy loss is determined by a TOF measurement. This detector has to meet many demanding requirements, and up to now, not all of them could be met satisfactorily. This led to a continuing development of ion detectors within the scope of this thesis. Since the first measurements, continuing improvements have also been made to most other aspects of the experiments: the heating laser, all diagnostics, the timing, the targets, and the overall precision of the measurements were all greatly improved during the past several years.

4.2.1 MCP and MSP detectors

At the beginning of energy loss measurements at the Z6 area, a MCP (Multi Channel Plate) detector was used. This detector type is described in detail in [Sue99] and [Ro97]. Some of these early measurements [Ro97] indicate that an inhomogeneous spatial laser profile causes problems. If the laser profile is not homogeneous, it leads to hotter and colder zones within the plasma. In this case, the laser profile was ring-shaped, so a possible explanation of measurements at that time was that part of the ion beam bunch passed through the ring zone of very hot and dense plasma, experiencing a high energy loss, while ions passing through the comparatively cold center of the target would experience an energy loss close to that of the cold foil.

In response, changes were made to the laser system to ensure a more homogeneous profile, including the addition of a randomizing phase plate.

It is necessary for the data analysis that the ion pulse passes the three-dimensionally expanding plasma exactly along the axis. The plasma is not homogeneous, so any deviation from the axis leads to deviation in the line density of the plasma. Consequently, the ion beam diameter must be made as small as possible. This demand may be somewhat lessened by the use of a fairly large (on the order of mm^2) laser-irradiation area and a homogeneous laser profile using the phase plate which ensures a plasma ablation as homogeneous as possible around the axis, but even then it is necessary to keep the ion beam diameter small. However, the ion optical systems are only able to focus this beam onto a minimal diameter of more than 2 mm^2 at the target. The only solution would have been to reduce the beam size using an aperture in front of the target, but this would reduce the number of particles available for measurement. At that time, this was not feasible

because the MCP detector is not sensitive enough to detect ions with low beam currents corresponding to only several hundred particles per bunch at the large distance which was necessary to ensure that the detector would not be incapacitated by the x-ray signal. It was discovered that the MCP detector was, in several ways, not ideally suited to the task. The shape and width of the signals made the data analysis very difficult.

In order to increase the precision of stop detector measurements, the MCP detector was exchanged for a micro sphere plate (MSP) detector.

The x-rays coming from the plasma 'blinded' this MSP for so long that this rendered the detector unable to detect ions within the most interesting temporal range. As a result, the detector, which was at first closer to the target, was moved further away. The drift space between target and detector was increased so much that the difference in flight times between the ions and the x-rays also increased until the signals of ions which had passed the plasma were no longer within the x-ray-induced dead time of the detector.

However, this had the disadvantage of increasing the loss of particles due to the longer beam line, thus worsening the signal-to-noise ratio of the ion signals on the detector. Fig. 4.4 depicts one of the main reasons why a longer drift space leads to particle loss.

All ion optic components within an accelerator beamline are designed to operate at a certain charge state of the ions. If ions of a given charge state are focused by a quadrupole multiplet, the same quadrupole multiplet will not be able to focus ions of a different charge state with the same focal length. This is illustrated in fig. 4.4.

In the case of a longer beamline with multiple quadrupole units, these transmission losses of particles not reaching the next quadrupole are increased at every quadrupole, since the beam after the first quadrupole is already split into different charge states at different angles. Small differences in charge state build up increasingly large differences in focal lengths. The longer the drift space behind the target, the more focusing magnets are needed in order to hold the beam together, and the more difficult it is to keep the beam transmission from deteriorating

Passing through a plasma changes the charge state of the projectile ions, so that there is always a mixture of different charge states coming out of the plasma. Moreover, this charge state distribution is a function of time. This has been previously investigated at Z6, see [Sue99].

The first energy loss experiments at the Z6 experimental facility within the scope of this thesis were carried out using this MSP detector as an ion TOF detector. Fig. 4.5 shows a typical image from those early measurements. Unfortunately, because our experiment is not allowed to request beamtimes on its own, we were forced to work at the same time with another research

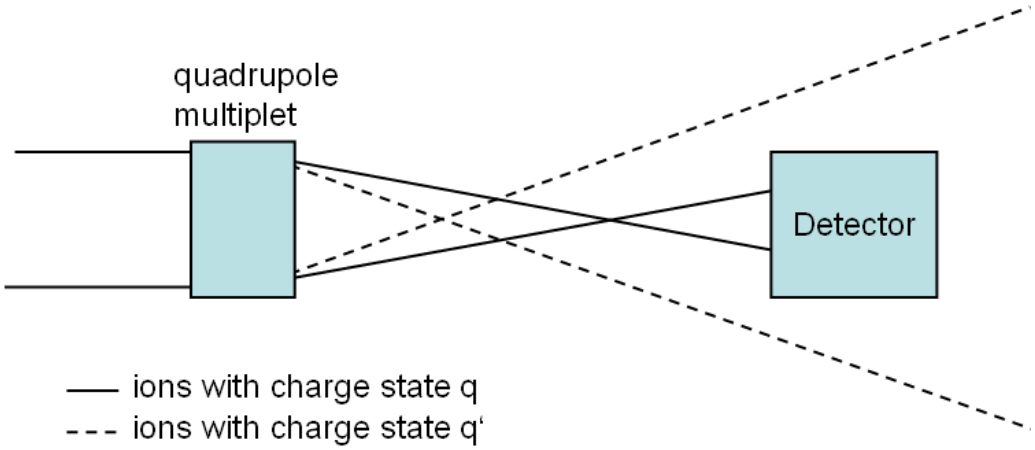

Figure 4.4: Focusing ion optics are designed for a certain charge state of the projectile ions. Ions with a different charge state will be focused more strongly or more weakly, so some ions which are focused 'wrongly' will be lost.

group which required one of the RFQ-frequency ion sources, so the peak-to-peak distance between pulses was 27 ns.

It is interesting to note that with the onset of the plasma formation, there seems to be at first a loss of ions, resulting in a much smaller peak which still experiences a delay corresponding to the energy loss in the cold foil, then a 'double peak' with two maxima located on the vacuum and the foil value. Further to the right, the maxima are approaching the values calculated for vacuum, with a slight delay, which is expected in a very diluted plasma. The lifetime of the dense plasma is on the order of 30 ns.

The delays corresponding to this measurement are depicted in fig. 4.6. Here, it becomes even clearer that these measurements were taken with one of the 'slow' ion sources, with an ion pulse peak-to-peak distance of 27 ns. With a plasma life time of 30 ns, only one peak is definitely within the lifetime of the plasma.

These are interesting results, but in the course of the data analysis, it was found that it was difficult to interpret the data because it was not possible to discern the detector response function from the shape of the ion bunch itself. The MSP detector produces signals which are fairly long, so if the distance between two ion pulses is very short, as it may be with the onset of delays due to suddenly increased energy loss in the plasma, there is a chance of overlapping pulses which cannot be properly analyzed. Additionally, the ion

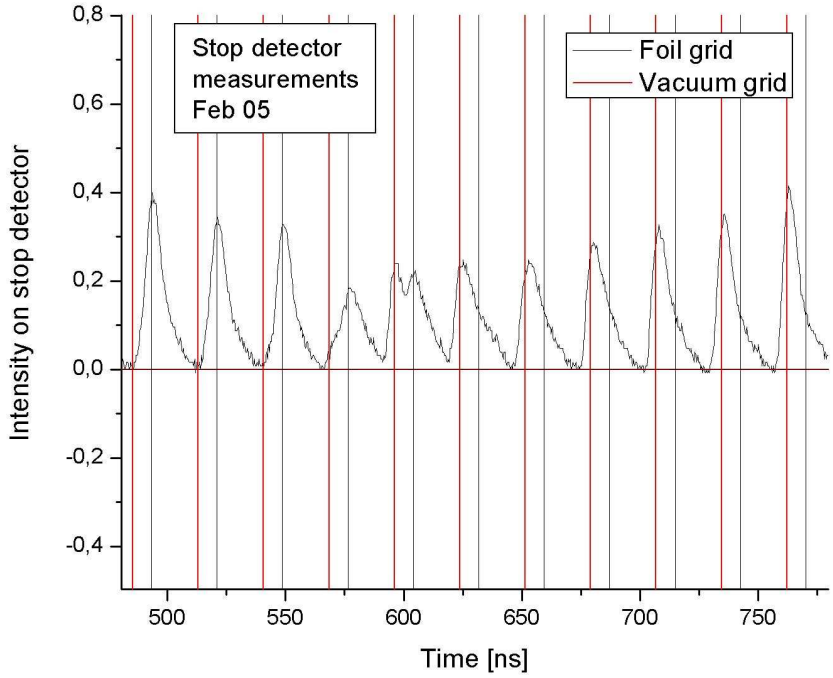

Figure 4.5: This image shows one of the earliest measurements made during the work on this thesis. The double peak structure of the fifth peak from the left is clearly visible. The black lines show the location of the peaks extrapolated back from the vacuum value, the red lines show the location of the peaks with constant energy loss due to the foil.

bunches apparently change their longitudinal shape during the interaction with the plasma, which would yield very important information if it were possible to eliminate detector effects on the pulse shape.

The detector signal is always a convolution of the detector response to a single particle and the actual pulse shape of the ion beam micro bunch envelope. The pulse shape of the undisturbed micro bunch can be approximated by a Gaussian or cos^2 function, as described in sect. 3.1. The detector signals of these bunches show a convolution of this Gaussian and the detector response function, but it is not possible to calculate the detector response function from this scarce information, as there is no exact data on the undisturbed pulse shape available. In order to be able to discern the detector response function from the shape of the bunch envelope, the detector re-

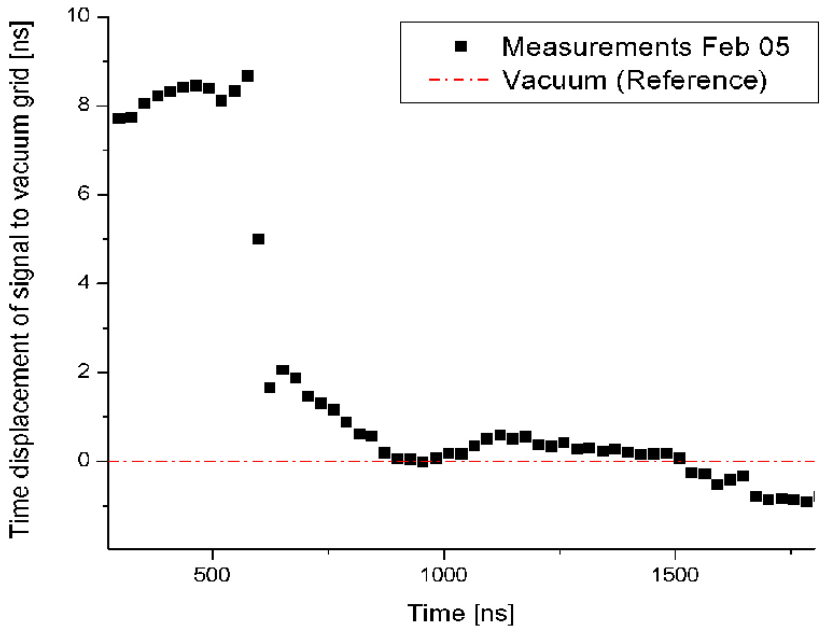

Figure 4.6: Temporal development of the pulse delay, which is closely related to the energy loss. As expected, the plateau on the left corresponds to the constant delay in the solid foil phase. The fluctuation is within errors. On the right, the data approaches the vacuum value, with the intermediate stage of steadily decreasing energy loss in diluted plasma or gas in between. Unfortunately, the temporal resolution is not large enough to permit closer investigation of the area between the solid foil stage and the gas stage - here, only a single data point is available, and this is the double peak structure mentioned in 4.5. This is numerically treated as a single peak, thus showing the almost exact average between foil and vacuum values.

sponse function to a single particle must be known. Within the scope of this thesis, the MSP detector has been tested using an Alpha particle radioactive source, but these tests turned out that the MSP is not sensitive enough to respond to a single alpha particle from the alpha source available. So, the single particle response could not be determined and the detector signal thus could not be de-convoluted into its component parts.

Another problem already encountered with the MCP was also still present with the MSP: the necessity to assure a fairly large amount of ions reaching the detector in order to maintain an acceptable signal-to-noise ratio. The use of a 300 μm beam aperture still remained unfeasible with the MSP detector.

The problems encountered with the MSP measurements led to the search for alternative detectors and eventually the development of a new diamond-based detector which is much more sensitive than the MSP, less vulnerable to the x-ray flash and can cope with an entire long macro bunch signal at 108 MHz without showing saturation effects.

4.2.2 CVD Diamond detector

Extensive research on new detector types and materials [Wam06] indicated that a polycrystalline diamond CVD (Chemical Vapor Deposition) detector would be the most promising candidate for a new, better stop detector.

Since there was no detector commercially available to suit our needs, a new stop detector had to be specifically designed and constructed from scratch.

Basically, the central component of a polycrystalline CVD detector is a polycrystalline diamond plate. This diamond plate is created using microwave CVD, which means that a plasma of methane and hydrogen vapor is brought in contact with a monocrystalline silicon wafer and gaseous carbon, and this is irradiated by microwaves. The radiation creates methane radicals and atomic hydrogen, who are very reactive and ensure that of the carbon deposited on the wafer, only diamond as the most stable configuration is present. Due to different lattice parameters of diamond and silicon, the resulting layer of diamond is formed out of many separate microcrystals, thus 'polycrystalline'. A REM photography of such a polycrystalline diamond plate can be found in [Wam06]. Monocrystalline diamond was ruled out mainly due to financial constraints, but also because the maximum usable area of monocrystalline plates was, at that time, not big enough for our needs.

The diamond plate then has to be enclosed by electrodes on both sides, similar to the design found in silicon semiconductor detector systems. The main difference between diamond and silicon is that diamond is a wide band

gap semiconductor, which means that diamond has an energy gap of 5.45 eV between valence band and conduction band, the highest of all materials suited for semiconductor applications.

Even under the best of conditions, it is impossible to create a 100% pure diamond plate; there are always defects and some impurities in the form of other atoms within the lattice. These atoms act as centers of recombination or 'traps' for the electron-hole pairs created by ionizing radiation, which affects the ability to act as a detector for ions. However, these traps can be deactivated by irradiating the diamond detector with ultraviolet radiation or electrons for longer periods of time. After that, the efficiency of the detector is greatly improved; this is called the "Priming" process.

Research on these effects [Beh98] concludes that polycrystalline CVD diamond can be used as a semiconductor detector for ions under two premises: First, that the defects caused by impurities are deactivated prior to the measurement using the Priming method, and second, the ions to be detected generate a homogeneous ionization density within the diamond.

In order to verify the second condition, calculations were made [Wam06] using the SRIM code [Zie03] studying the energy deposition and range of several ion species in diamond. The results are depicted in Fig. 4.7.

The maximum range of the ions were 44 μm for carbon (the lightest ion), 32.4 μm for neon, 28.8 μm for argon and 27.7 μm for krypton. So, for the detector to satisfy the condition of homogeneous ionization, it must be thin enough depending on the ion species used. The slowly rising, but fairly constant energy deposition of the ions within the target before the Bragg peak (i.e. the region of maximum energy deposition) ensures homogeneous ionization. The maximum thickness for the detector must be less than the distance to the Bragg peak for the ion species used as projectile ions.

So, four detectors were built: P1 (13 μm), P2 (19 μm), P3 (20.5 μm) and P4 (60 μm), each with a detection area of a 10 mm by 10 mm square. Detectors P1 through P3 would be suitably thin for all ion species in Fig. 4.7, while P4 could be used to study the effects of a thicker detector on the measurements.

The main difference between P3 and the other three detectors was the choice of material for the electrodes. P3 was sputtered on both sides with a single 100 nm layer of aluminum, while the other three were sputtered with a triple layer: first 20 nm titanium, then 30 nm platinum and, last, 100 nm gold. All four were heated to 500C for 10 minutes in a nitrogen atmosphere to remove contamination on the surface.

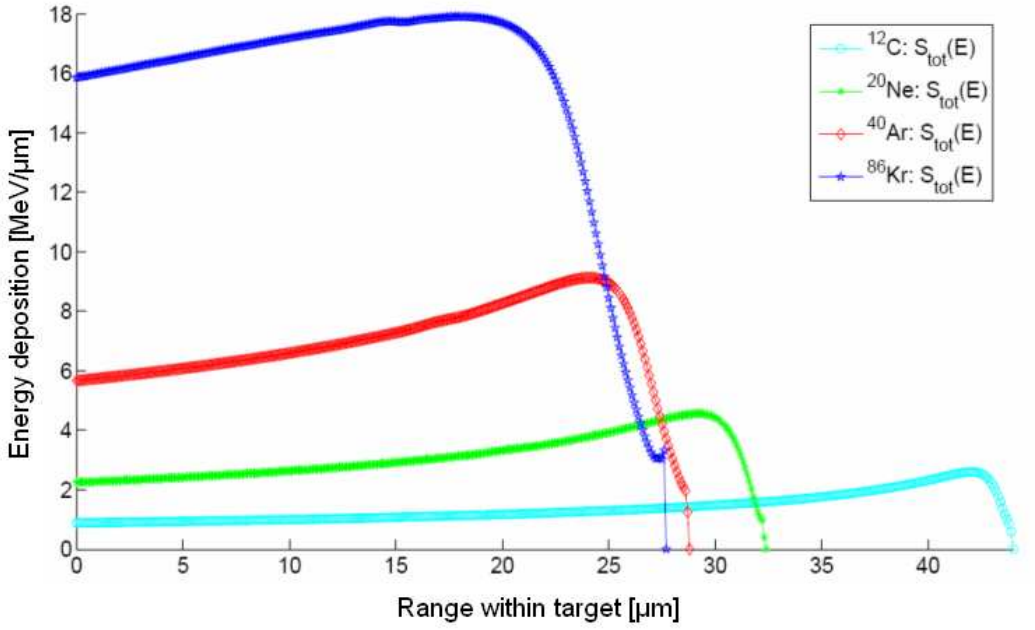

Figure 4.7: Energy deposition of ions at 5 MeV/u in diamond, calculated using SRIM. Ion species are, graphs from top to bottom: krypton, argon, neon, and carbon. [Wam06]

4.2.3 Results of detector tests

The detectors were then extensively tested in a beamtime using a chromium beam, which has an atomic number of 57 and thus ranges between argon and krypton. It was shown that the detector must not be thicker than the maximum range for homogeneous ionization, as was discussed in the previous section.

A direct comparison was made between detectors P1, the thinnest, and P4, which is about twice as thick as the maximum range of the chromium ions, so they would be completely stopped within the detector material. The results show that during one macro pulse from the accelerator, the micro bunch signal amplitudes of P1 remain constant within statistical fluctuations mainly due to fluctuation of the ion source, while the micro bunch signals of P4 exhibit a decrease in amplitude over the entire interval studied. This is a detector effect, as there is no physical evidence and no reason that the signal amplitudes should change.

Also, the widths of the pulses were compared. Basically, both P1 and P4 show signals that closely resemble the expected shape and width of the micro

bunches (cf. Fig. 3.2). However, the signals of P4 have a lower width, but at the same time, are smaller than those of P1, due to the lower capacity of P4.

P2 and P3, the two detectors with 19 and 20.5 μm thickness but different electrode materials, showed optimum behavior in respect to the desired high amplitudes and small widths of the signals.

Improvements achieved by the use of the diamond CVD detectors

The temporal resolution required of the stop detector is also attained by the new diamond detectors. In order to precisely measure delays of less than a nanosecond, as are expected in the energy loss measurements, the detector should have a temporal resolution of a few hundred picoseconds. Additionally, the dead time of the detector must be very small, on the order of picoseconds. This is the case.

One main reason to introduce a new detector type was the inability of the MCP and MSP detectors to cope with extremely low ion beam currents.

An ion beam micro pulse typically consists of the order of 10^5 particles, and the beam current in front of the target is on the order of several μA. If an aperture of several 100 μm in diameter is introduced to reduce the ion beam diameter further than the 2 mm^2 achievable with UNILAC ion optics, most of the beam is cut off. Additionally, there are losses due to the long drift space between target and stop detector, as described at the beginning of this section. Depending on the ion source used and on the ion species, the number of particles per micro bunch that arrive at the detector when using a 300-500 μm aperture ranges between 200 and 1000 particles, which corresponds to beam currents of several hundred nA. Most detectors are not able to detect such low-current beams at all.

Tests showed [Wam06] that even with beam currents as low as 300 nA, the new detectors produced clear signals of 2-3 V in amplitude. This was a major improvement compared to the previous detectors, which would not have produced any signals at all with such a low beam current.

Additionally, the x-ray flash from the plasma and the resulting saturation of the detector was a problem, previously. The diamond detectors are also able to detect x-rays, as it is desirable because the x-ray signal recorded by the stop detector is used as an additional marker for the timing. However, they are much less seriously affected by the x-rays and resume their normal operation much earlier than their predecessors. They do not even reach saturation most of the time. Sometimes, the micro bunch signals remain discernible throughout the entire x-ray signal, as is shown in [Wam06]. This enables us to maybe decrease the distance between detector and target

again in the future, as it was only increased because of the inability of the MCP/MSP detectors to recover from the x-ray flash in time, cf. section 4.2.1. The longer distance led to the problem of an increased probability of particle loss, which becomes important again in the most recent results.

With the new diamond detector, at least three major improvements have been made.

First, it was possible to obtain more information on the single-particle response function using an alpha source. So, a new method of analysis could be employed, regarding each peak on the ion detector as a convolution of the ion beam bunch shape and the single-particle response function, thus separating physical effects from the technical issues. Since both functions are approximately known, they can be separated during analysis. This had not been possible with the MSP detector, as it proved not to be sensitive enough to react to a single alpha particle, cf. section 4.2.1.

The second improvement is due to the increased sensitivity of the detector. With the old MSP detector, the ion beam had to be quite large in diameter in order to produce a signal of sufficient intensity on the detector. However, it is preferable to reduce the ion beam diameter as much as possible, to avoid effects such as different parts of the beam passing through plasma of different temperatures and densities. With the new detector, it was possible to insert a 500 μm aperture in front of the target, so the ion beam diameter could be reduced to approximately that value, while the signals on the detector are still suited for data analysis.

Last, the x-ray flash has become less of a problem, which enables us to be more flexible in the placement of the stop detector in the future.

Chapter 5

Measurements using MSP and diamond detectors

5.1 Measurement of plasma speed

In the first experiments, other diagnostics were included to measure plasma conditions. A fast CCD camera (model DiCam Pro) with an exposure time of 5 ns was used to observe the plasma in the optical range. This is done in order to assure that plasma expansion is symmetric around the axis. Also, other undesired irregularities, such as the laser accidentally hitting the target holder, would be seen by the cameras. Figure 5.1 shows this image in the optical range. The target ladder, which can be seen on the image as a dark vertical structure, has a width of 2 mm.

Clearly, two areas can be distinguished: a bright, inner plasma region and a less bright outer region. Both expand approximately spherically, as is indicated by the circles. This is the desired symmetrical plasma structure along the axis.

Besides their use to verify the symmetrical expansion of the plasma, these images can also be used to estimate the speed of the expansion, as the camera timing in relation to the laser pulse is known. An intensity profile created from the image is shown in Fig. 5.2. Expansion speeds were calculated from this profile. However, as the image is an integrated image over 5 ns, the speed calculated is but a rough figure.

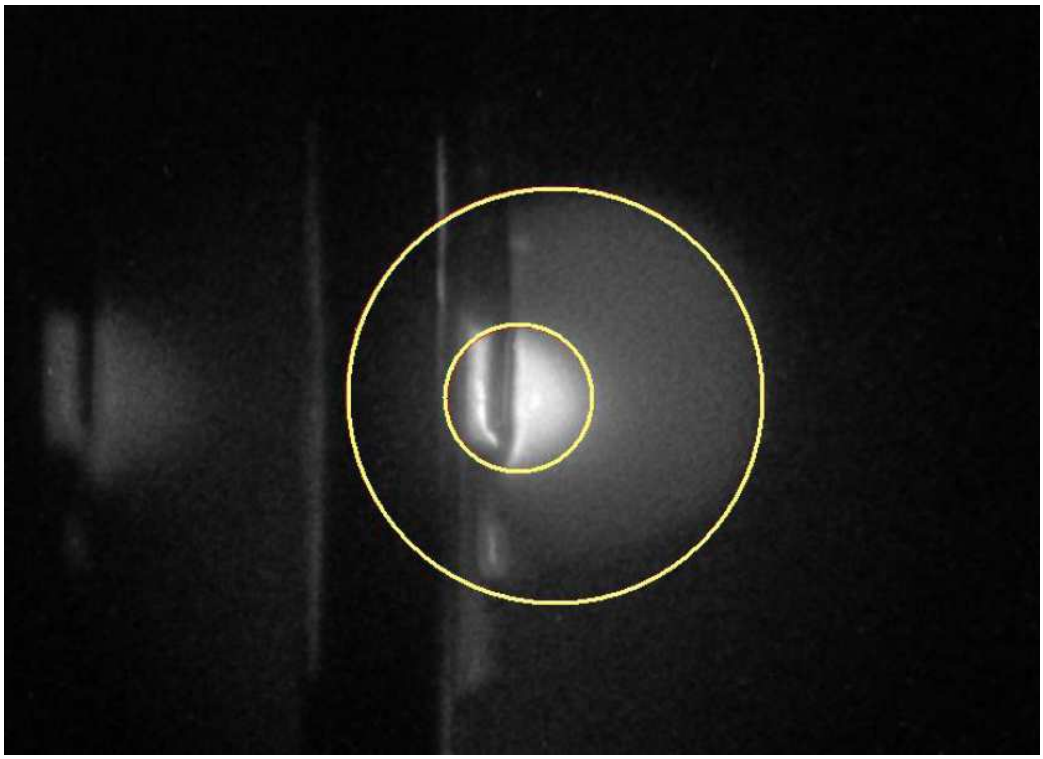

Figure 5.1: Expanding plasma in the optical range. The dark vertical structure is the target ladder; the target holder is visible on the right side of it. In the middle of the smaller circle, the carbon foil is located.

5.2 Early measurements using the MSP detector

Since the new CVD diamond detectors were developed within the scope of this thesis, first measurements were carried out using the MSP detector. One of the earliest energy loss experiments within the scope of this thesis was done using the MSP stop detector, an argon ion beam, a 50 J nhelix beam and carbon targets with a foil thickness of $300\mu g/cm^3$. The ion beam diameter was 2 mm, as at that time, the beam diameter could not be reduced further by an aperture due to the MSP stop detector being unable to cope with much smaller beam currents. The delay between laser and ion beam was varied in order to be able to temporally sweep through an entire micro bunch, albeit in different measurements. The results are shown in Fig. 5.3.

Common to all measurements is a decrease in amplitude of the signals with the onset of the plasma. However, a split-up of the following peak or

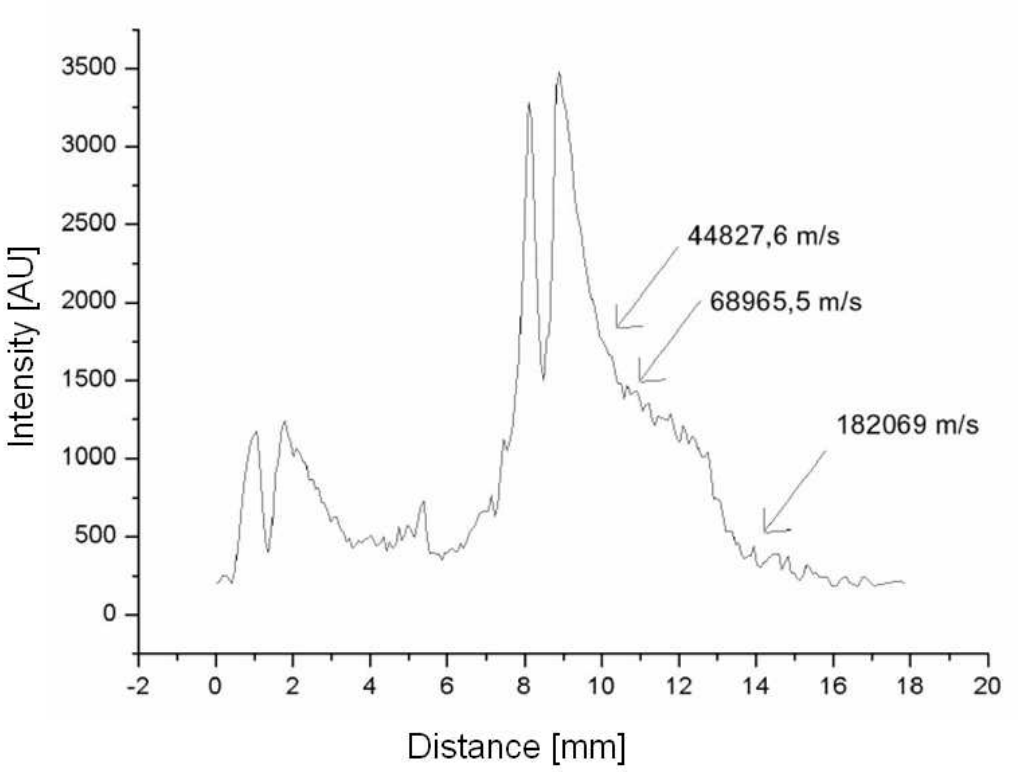

Figure 5.2: Line profile of fig. 5.1. Expansion speed was calculated for both the bright inner plasma and the outer plasma. [Sch05]

peaks, as was depicted in 4.5, can only be observed in the last five measurements. Then, the two maxima are located at delays corresponding to solid foil and vacuum values, suggesting that there are two different ion populations passing through different regions of the plasma, as was already speculated before. However, there was no clear connection to the laser profile.

The main result of these early experiments was the realization that a better ion detector would be necessary in order to study these effects in more detail and higher resolution, and to be able to reduce the ion beam diameter further to avoid inhomogeneities in the plasma, so the design and development of a new detector was started.

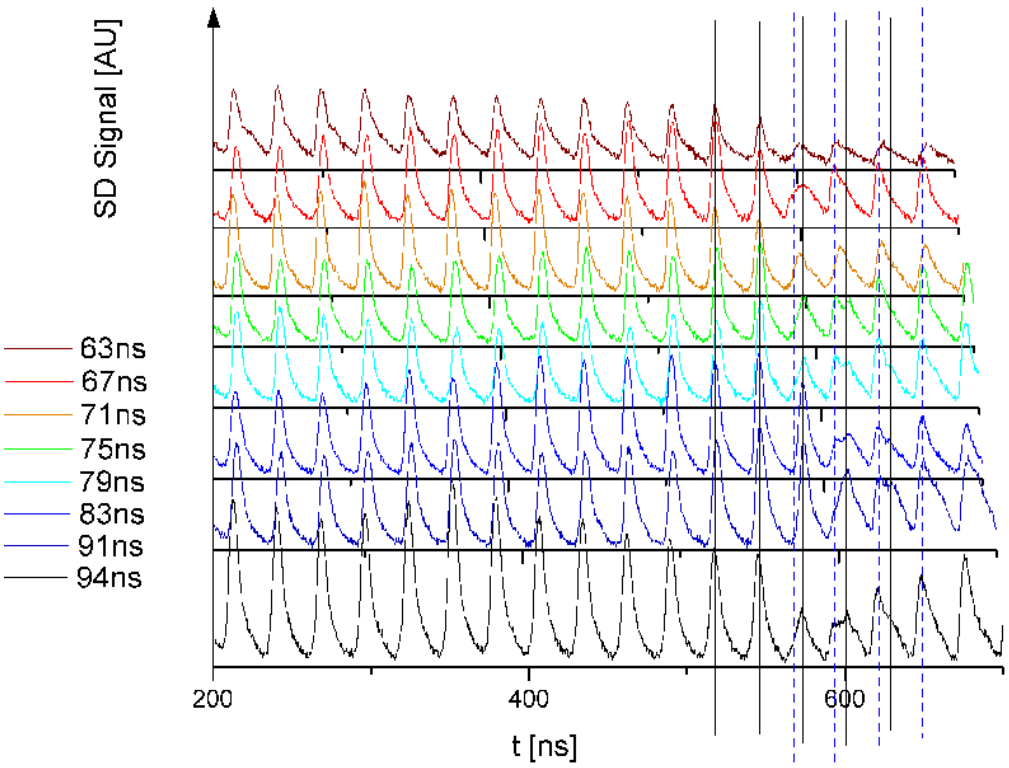

Figure 5.3: Ion signals taken with different delays of the laser beam in respect to the ion bunch. Values on the left correspond to the delay generator settings, so a value of 67 ns means a delay of +4 ns compared to the 63 ns measurement. Calculated vacuum values are given by the dashed lines, solid foil values by the solid lines. The laser energy was approx. 50 J, foil thickness $300\mu g/cm^3$. All graphs have been aligned to match the same grid as to make a comparison between the different delays easier.

5.3 Energy loss measurements with the diamond detectors

5.3.1 Energy loss of argon ions

With the present experimental setup, the temporal delay between laser and ion micro bunch can be shifted by one or more nanoseconds. If all other parameters are kept as constant as possible, results from different measurements with different delays may be incorporated into one image. This improves the temporal resolution to 1-2 ns instead of a minimum of 9.22 ns, as dictated by the ECR ion source.

However, this improvement also means that systematic errors due to using data from different measurements are accepted. While the experimental conditions are fairly reproducible, there are always small variations, for example in the surface structure of the target foil.

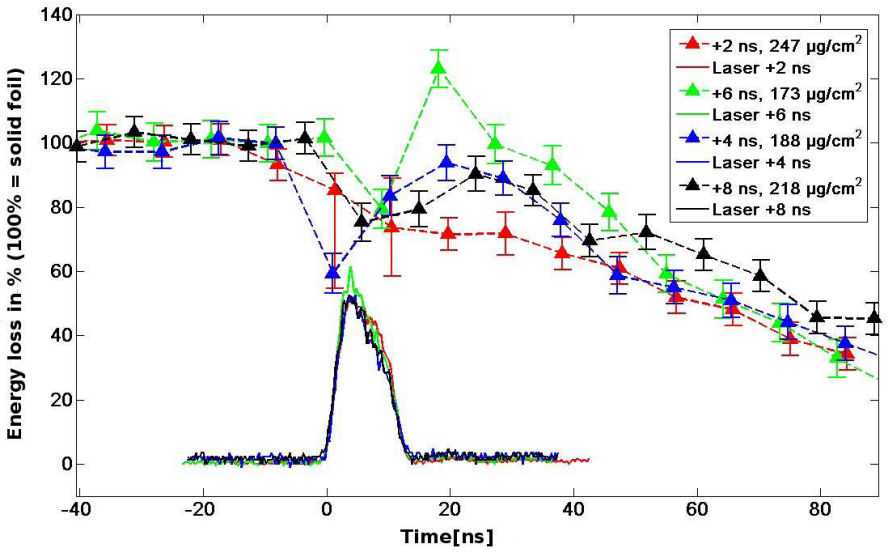

Figure 5.4: Energy loss measurement of argon ions with target foils of approximately 200 μg/cm^2 density [Fra08]

Fig. 5.4 shows such a composite image of four measurements, taken with time shifts of 2 ns in respect to each other. In the bottom of the image, the corresponding temporal laser profiles are shown in solid lines. They are all very similar, so that most of the lines overlap. The dashed lines above the laser profiles each represent one energy loss measurement. The foils show a variation in thickness which cannot be eliminated in the manufacturing process. The foil thickness values given in the image are those calculated directly from the measured energy loss of the ion beam in the cold foil. The error bars represent three errors: first, the error made in defining the exact location of the ion signal peak by using a fit, second, the error in matching the detector signals to the 108 MHz frequency of the accelerator which is the frequency of the ion bunches, and third, the error in setting up the vacuum reference. The systematic errors due to the use of different measurements are only taken into account by making clear which data points belong to which measurement, so systematic deviations can be seen easily.

In this image, some differences can be observed between the different measurements, but also some common characteristics. On the left, the constant

energy loss in the cold foil is clearly visible for all four measurements. The graph has been adjusted for the slightly differing foil thicknesses by using a relative scale, 100 percent corresponding to the calculated energy loss in the solid foil of the respective thickness.

To the right side of the graph, all measurements show the behavior expected during the gas/thin plasma stage. As the plasma is becoming thinner and the line density on the axis is reduced due to material expanding away from the axis, there is a steady decline in energy loss. With increasing time, this slowly approaches the vacuum value of zero energy loss.

With the rising flank of the heating laser pulse and thus the onset of the plasma, three of the four measurements show an unexpected drop in energy loss, followed by a rise. This region during and shortly after the laser pulse is the plasma region, the most interesting region in our measurements. Due to the ECR ion source frequency of 9.224 ns, only one or two data points in each measurement are within this plasma region. This led to the idea of combining data from several measurements in order to improve the resolution.

All measurements except the one at +2 ns delay (red line) show a drop in energy loss which is approximately coinciding with the laser pulse duration, then a rise. The +6 ns delay measurement (green line) is the only measurement where, after the drop, the energy loss increases again to a higher level than that of the solid target; both other measurements remain at a peak value a little below the solid foil value.

The red line measurement is unusual: it does not show the drop and subsequent rise in energy loss like all three others. However, the two points within the plasma region suffer from very large errors, which may obscure such details in structure. Within these errors, many scenarios are possible.

Interestingly, the 'red' measurement is the one with the thickest target foil within the set of four: 247μg/cm^2, with the others being 218 μg/cm^2, 188 μg/cm^2 and 173 μg/cm^2. The other unusual measurement, showing a rise in energy loss above the solid foil value, was the thinnest foil used. The 'blue' and 'black' measurements, which show a strong similarity to each other, are the two intermediate thicknesses. This leads to the conclusion that the thickness of the foil plays a very important role in these measurements.

Several considerations in previous years led to the use of foils with a line density of 200 μg per cm^2, almost exclusively. The line density is the integral over the density of matter an ion beam of given diameter passes on its axis.

$$\rho_{line} = \int_{x_i}^{x_f} \rho(x) dx \tag{5.1}$$

Here, the values x_i and x_f are the beginning and end of the matter dis-

tribution, respectively. If the plasma expansion is one-dimensional along the axis, the total amount of matter on the axis is always constant, thus the total line density also remains constant. In order to ensure this, the present setup at Z6 was chosen. Unlike previous experiments who used a plasma expanding at a 90° angle to the ion beam, the collinearity of plasma expansion and ion beam makes it much easier to develop theoretical descriptions of the interaction.

With the new CVD diamond detector, again measurements were made to study the effects of foil thickness.

In figure 5.5, the delay between laser and ion beam bunch was systematically shifted, and a foil with a thickness of approx. 200 μg/cm^2 was used. In the bottom (black line) measurement with a delay of 8 ns, there are clearly two peaks, the one at about 10470 ns and the following peak, whereas in the topmost measurement, the second peak is only visible as a bump on the flank of the preceding peak.

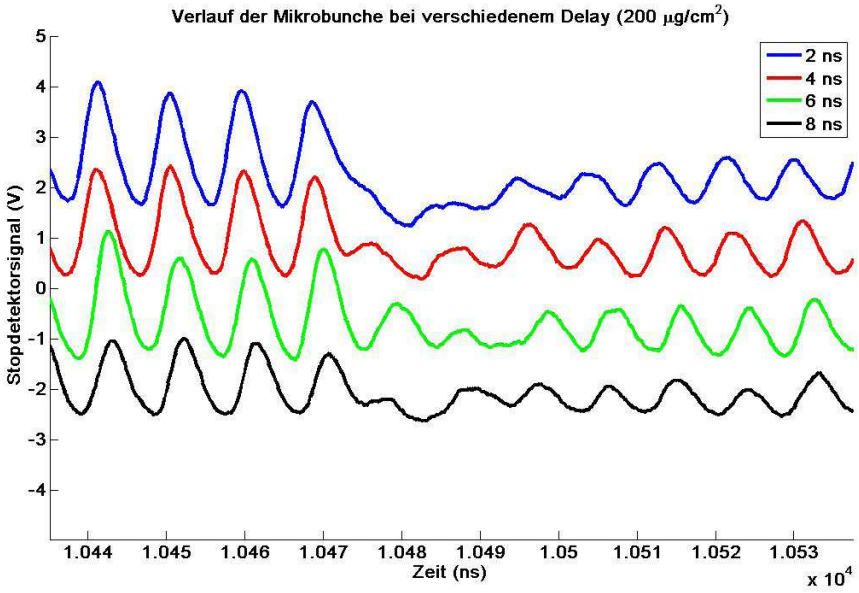

Figure 5.5: Systematic measurements with a foil thickness of approx. 200 μg/cm^2 show that when shifting the delay between laser and ion beam bunch, the timing may cause two peaks to occupy almost the same temporal position and merge into one, so that apparently one of the peaks disappears. [Fra08]

This merging of two peaks into one makes it very difficult to gain accurate information about the shape of the pulse and the peak location of the second peak, which is the first peak in the plasma region and thus the most

interesting. The large error bars in the 'red' measurement in fig. 5.4 were a result of these difficulties.

As a consequence, in the most recent experiments, this problematic value of 200 μg/cm^2 was abandoned, and thinner 100μg/cm^2 foils were used, which avoids the problem. With the MCP/MSP detectors, this had not been possible because these detectors were not sensitive and exact enough for measurements with these thin foils.

In order to further research the effect of foil thickness on the results of energy loss measurements, the energy loss of argon in thicker foils ranging from 400 μg/cm^2 to almost 500 μg/cm^2 was studied, see fig. 5.6.

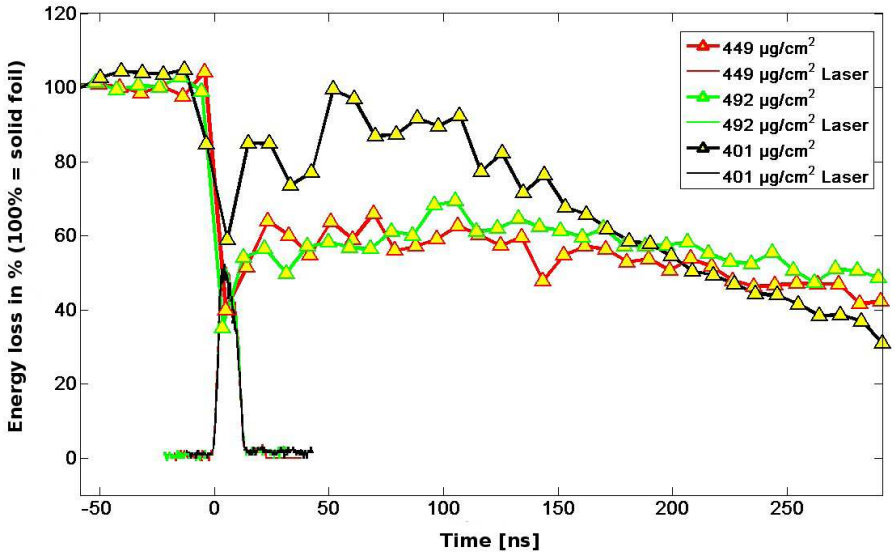

Figure 5.6: Energy loss measurement with a 400 μg/cm^2 foil [Fra08]

These results are in accordance with the previously shown measurements. Here, all three graphs show the drop in energy loss roughly corresponding to the laser pulse duration. However, as before, within the plasma region there are only up to two data points in each measurement, so the effect of the 'missing' drop in the 200 μg/cm^2 measurement could easily have been created by the large errors for the first plasma peak with the problematic foil thickness of 200 μg/cm^2.

As before, the two thicker foils (green and red line) show a very low rise in energy loss after the drop, while the thinnest of the three foils reaches the highest energy loss value, but remaining below the solid density level.

It is important to note the different time scale here compared to fig. 5.4, which shows a time up to about 90 ns after the laser pulse. With the

thicker foils, the steady decline of the energy loss towards near zero did not start until about 150 ns after the laser pulse. Before that time, all graphs show some fluctuation, suggesting that the thicker foils are also more prone to cause inhomogeneities in plasma expansion. Also, the expansion of the matter away from the axis is much slower than with thinner foils. Even after several microseconds, the line density on the axis had not completely vanished, which is detrimental to the 'vacuum stage' reference method used in these experiments and described in detail in section 4.1.1.

All these considerations led to the decision to use thin foils with 100 μg/cm^2, as these proved to be best suited to the needs of the energy loss measurement. With these foils, the line density vanishes sufficiently at later times in order to establish a good reference. Also, the energy loss in the cold foil is smaller, resulting in shorter delay times than with thicker foils, which eliminates the problem of the last peak in the solid foil stage and the first plasma peak colliding, as was shown in fig. 5.5. Furthermore, the variation in foil thickness due to the manufacturing process is a percentage of the desired thickness, thus thinner foils result in less absolute variation in thickness, which is an additional advantage.

With 100 μg/cm^2 foils, systematic differences between several measurements became so small that actually data from four different measurements could be combined into a single data set, as shown in fig. 5.7.

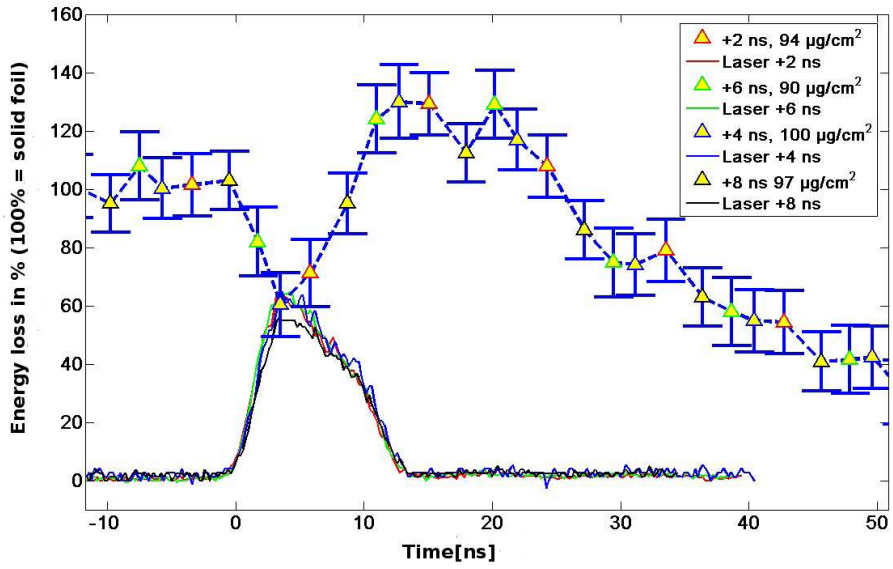

Figure 5.7: Composite image of energy loss data from four different measurements using foils with approx. 100 μg/cm^2 thickness [Fra08]

As in figures 5.4 and 5.6, a relative scale is used to compensate for the variation in foil thickness, with 100 percent corresponding to the energy loss in each cold foil. The data points from the four different measurements are indicated by their colors. Small systematic differences between the four data sets are visible, as for example the red data points are always slightly higher than the others, but the overall difference between the four plots is very small.

Here, with the increased temporal resolution, the structure of the drop in energy loss is very similar to the inverse of the laser profile, which is shown beneath the energy loss graphs. This suggests that this behavior is linked to the temporal laser profile. However, up to now there is no concise explanation or theory as to the mechanisms leading to this drop in energy loss.

To the right of the drop, all data show a rise in energy loss well above the level of the solid foil. This is again consistent with previous figures 5.4 and 5.6, where only the thinnest foil in fig. 5.4 showed this behavior, while the energy loss in thicker foils after the drop did not reach the solid foil level at all and was even lower in this temporal area.

5.3.2 Energy loss of calcium ions and changes to the laser direction

In the search for an explanation to the drop in energy loss observed in the experiments described above, it was speculated that laser fields could be the reason that the ion beam bunches in question were actually accelerated rather than decelerated. If that was indeed the case, the reversion of the laser impact direction would mean an inversion of the field also, so there should be a difference between the two laser directions.

In most experiments during the last years, the laser heated the target from opposite the direction of the ion beam. However, in the most recent beamtime, the setup was changed to accommodate also laser heating from the same side as the ion beam. Tests had been done in the past [Sue99] to check whether the energy loss was dependent on the direction of the laser beam. This was not the case then; however, we decided to repeat the experiment with our improved diagnostics and different laser.

It turned out that the setup with laser and ion beam coming from the same side is technically much more difficult to implement than the version with heating laser and ion beam coming from opposite sides. Ideally, the heating laser beam should be on the same axis as the ion beam. That, of course, is not possible, in neither setup, as it is not feasible to introduce optical elements such as mirrors in the path of the ions.

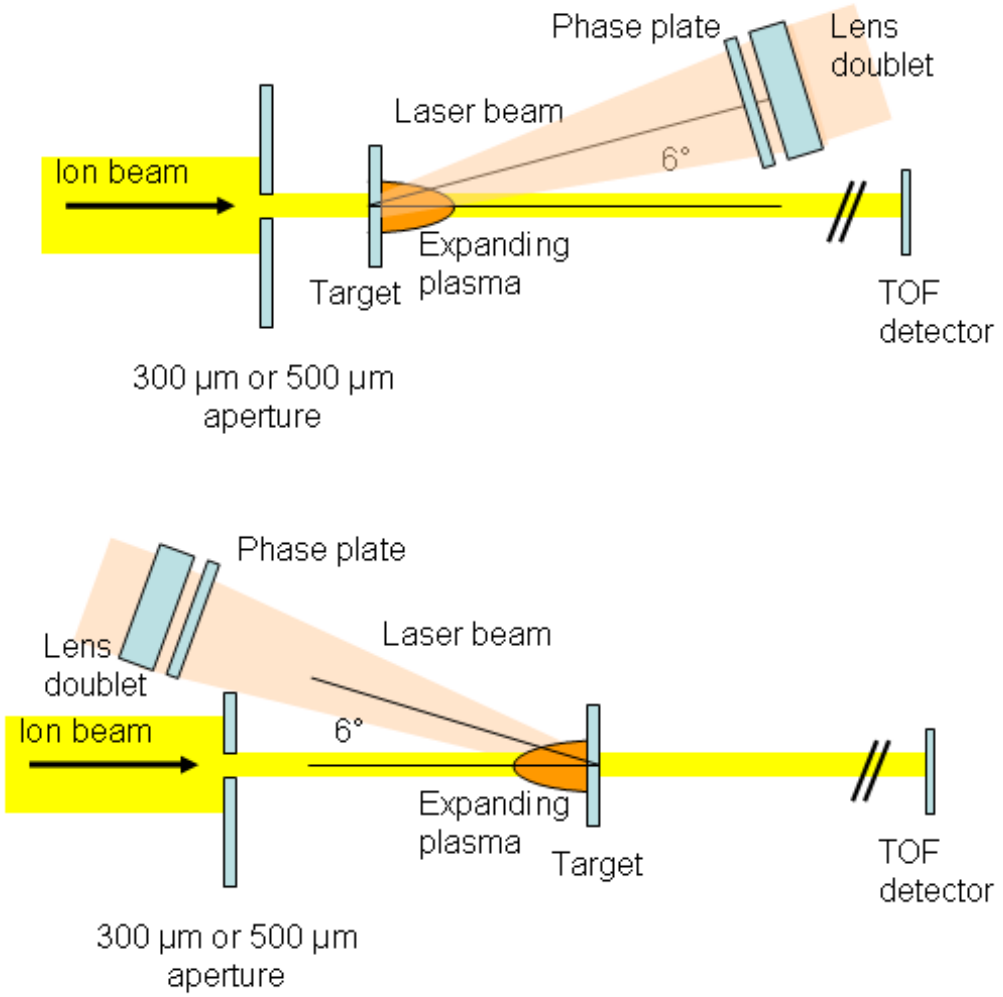

Figure 5.8: Schematic drawing of the two different setups used to study the effects of changes in the heating laser direction. Note that the images are not drawn to scale: the distance between target and TOF detector remains exactly the same. The distance from the aperture to the target was as close as possible in the respective setup, it differs by several cm.

In the setup with both beams on opposite sides, the laser beam is sent onto the target at a small angle to the ion beam axis, using a mirror located off the axis.

The most difficult obstacle was the newly-introduced aperture in front of the target. This aperture ensures one of the main improvements compared to earlier measurements, a small diameter of the ion beam, so it could not be removed. The aim of the reversal of the laser direction was to be able to compare this to the measurements with the laser coming from the opposite direction of the ion beam, so the aperture had to remain in its place in order to be able to compare the two setups.

This problem could be solved only partially. The aperture had to be placed a few cm further away from the target, otherwise the laser would hit the side of the aluminum plate of the aperture and create a plasma there, which was unwanted. Another problem was that during evacuation of the chamber, the setup shifted and had to be readjusted, so in many ways, this setup with laser and ion beam coming from the same side is unpractical and was only used for the tests whether a change in the laser direction would have an influence on the drop in energy loss.

In this beamtime, the energy loss of calcium ions was studied, because argon was not available. Also, in previous experiments, a random phase plate was included in order to homogenize the spatial laser profile. A homogeneous spatial laser profile ensures more homogeneous expansion conditions. However, during this beamtime, measurements were made with and without this phase plate in order to study another possible influence on the energy loss with the new diamond CVD stop detector and other improved diagnostics.

Fig. 5.9 shows the energy loss of calcium ions in a 200 μg/cm^2 foil. This image was made using data from only one measurement, so the energy loss is given on an absolute scale instead of a relative one. The drop observed in the previous experiments is visible also in this geometry, with the laser coming from the opposite direction. So, it cannot be an effect of the laser field, as this field is reversed now. As this graph only uses data from one measurement, the time resolution of 9.224 ns is low. However, this image is similar to corresponding graphs using foils of this thickness and argon ions in the previous geometry.

Fig. 5.10 also shows the energy loss of calcium ions in a 200 μg/cm^2 foil with the changed geometry, but additionally without the phase plate. The resulting image is similar to Fig. 5.9, which was created with the phase plate. However, due to the coarse resolution, a more detailed analysis of the shape of the energy loss curve is not possible.

In Fig. 5.10, the drop in energy loss is present as in all previous measurements with the CVD detectors. After the initial drop in energy loss, the

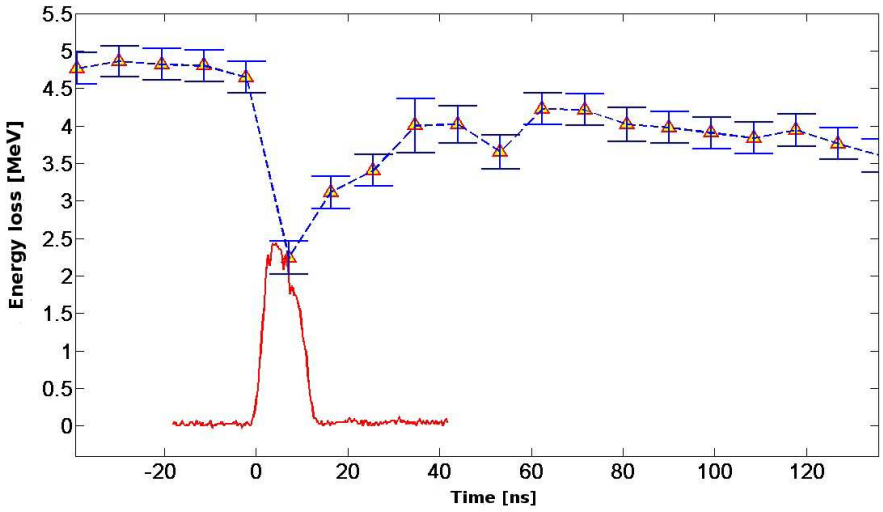

Figure 5.9: Energy loss of calcium ions in a 200 μg/cm^2 foil, with phase plate [Fra08]

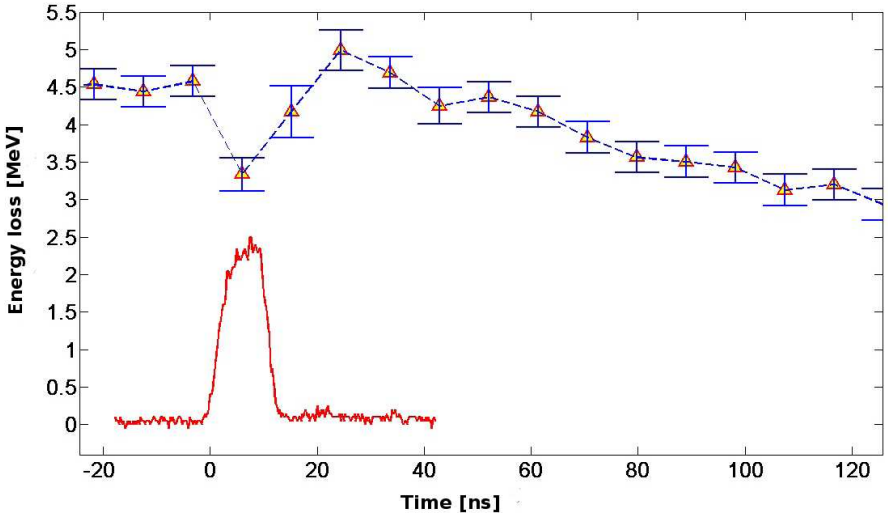

Figure 5.10: Energy loss of calcium ions in a 200 μg/cm^2 foil, without phase plate [Fra08]

energy loss rises above the solid foil level before beginning its slow decrease. Here, it would seem that the phase plate has the effect of intensifying the energy loss in the plasma, but more measurements would be necessary to further investigate this issue. It was not practical to attempt this in the changed geometry which is experimentally much more problematic than the 'normal' setup with the laser and ion beam from opposite sides.

The figures Fig. 5.11 and Fig. 5.12 show the energy loss of calcium ions in a 107 μg/cm^2 foil, with and without phase plate, respectively.

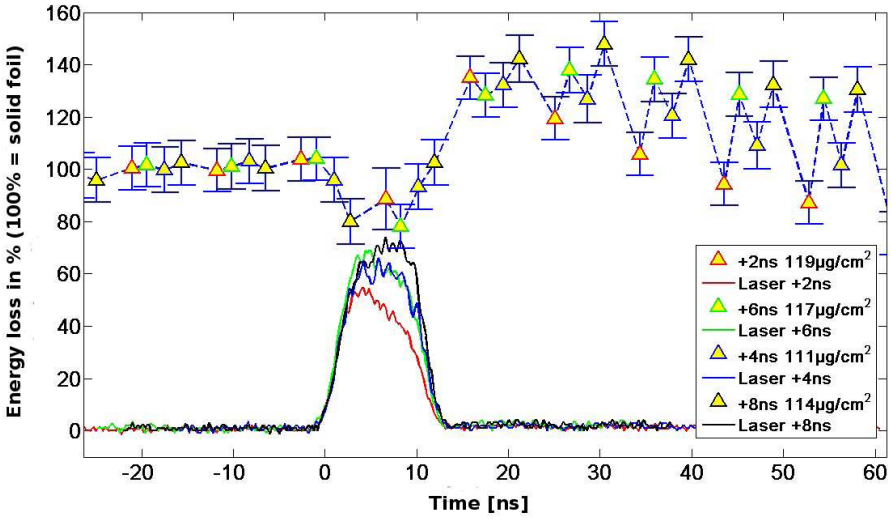

Figure 5.11: Energy loss of calcium ions in a 107 μg/cm^2 foil, with phase plate [Fra08]

Fig. 5.11 shows again a composite graph with data from four measurements combined in order to improve the temporal resolution. However, the four measurements can be clearly discerned, as the decrease in energy loss at higher times is slightly different for each measurement. This cannot entirely be attributed to the slight variation in foil thickness, although it is consistent with previous measurements that the thickest foil shows a lower rise and faster decrease in energy loss.

In the bottom of the image, the temporal laser profile is shown for all four measurements. Like in previous measurements with foils of this thickness and with argon ions, the drop in energy loss generally mirrors the shape of the laser profile. It is interesting to note that in the red measurement, which exhibits the lowest drop and lowest rise of energy loss of the four, the laser profile shows that the maximum laser energy had also been lowest. Additionally, the red laser profile does not exactly form a flat-top shape, but

shows a decrease in intensity. In contrast, the black laser profile is the one with the most intensity and also a good flat-top shape, and corresponds to the black measurement which displays the highest rise in energy loss after the initial drop. This suggests that there is a strong connection also between energy loss and both energy and shape of the laser pulse.

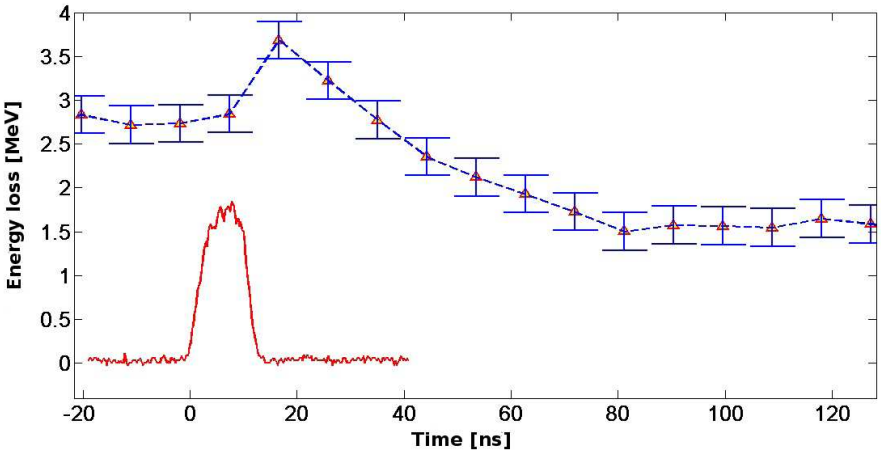

Figure 5.12: Energy loss of calcium ions in a 107 μg/cm^2 foil, without phase plate [Fra08]

Fig. 5.12, showing a measurement without the phase plate is unusual because it is the only one which does not show an initial drop in energy loss before the rise. However, the most likely explanation may be that due to the resolution of 9.224 ns, a sharp drop might have been lost between two data points. Other than that, there is yet no explanation for this missing drop.

5.4 Interferometry

The basic principle of any interferometric measurement is to divide a beam of light (e.g. laser) into a reference beam and a probe beam, let the probe beam pass the object to be investigated, and then let the two beams interfere with each other. From the interference pattern, deductions can be made about the refractive index of the object that the probe beam has penetrated. From this, it is evident that the object to be probed must be transparent to the light used for the probing. In the measurements described in this work, a green laser with a wavelength of 355 nm has been used.

In an interferometric measurement, the change in the refractive index of the probed material is made visible in the interference pattern.

Interferometric measurements can be used to gain information about the density of free electrons in a plasma, since this free electron density is related to the refractive index.

The refractive index of a plasma is given by

$$n = \sqrt{1 - \frac{\omega_p^2}{\omega_L^2}} \tag{5.2}$$

where ω_p is the plasma frequency (see Eq. 2.5) and ω_L the frequency of the laser:

$$\omega_L = \frac{2\pi c}{\lambda_L} \tag{5.3}$$

The plasma frequency is a function of the free electron density. If it is inserted in Eq. 5.2, it reads:

$$n = \sqrt{1 - \frac{\lambda_L^2 e^2 n_e}{\pi c^2 m_e}} \tag{5.4}$$

with e the elementary charge and m_e the electron mass. Since the laser wavelength λ_L is known, the refractive index n depends on the free electron density only. So, interferometric measurement of the refractive index of a plasma yields direct information about the free electron density of the plasma.

In the energy loss experiments, an interferometry setup is used to gain information about the free electron density in the plasma. A Wollaston interferometer is used. A Wollaston interferometer was set up with the frequency-tripled Geola (OS2) laser, cf. fig. 3.3.

The laser beam is frequency-tripled before entering the target chamber. The beam diameter is large enough so that the plasma region is completely penetrated by the beam. Also, a sufficient region without plasma (i.e., containing only vacuum) is encompassed, which is necessary to determine fringe shifts during data analysis, as there has to be a portion of undisturbed fringe visible in order to determine the shift.

After having passed the plasma, the beam is focused by a lens and then split into two beams by a Wollaston prism/crystal. These two beams are polarized perpendicular to each other, which are separated at a small angle.

Both beams pass a polarizer at a 45 degree angle. This is done to adjust the direction of polarization on the CCD chip of the camera, to improve the contrast. Finally, the beams pass an interference filter which has to be included here to protect the camera from stray light and from the much brighter light of the plasma itself.

The details of this interferometer can be found in [Pel05].

Using 2D interferometry data calculated by A. Pelka, the energy loss was calculated in 2D using a Matlab routine which was developed by A. Pelka and A. Schoekel.

Interferometry methods always need a reference of undisturbed fringes in order to be able to calculate the fringe shift. This can be achieved in two ways. Either, the field of view of the camera has to be chosen large enough that there are always areas without plasma and thus with undisturbed fringes, or a reference image has to be taken without any plasma. The latter approach was used in the last beamtimes, as this is the more practical one. The camera view can be chosen to contain the entire plasma without having to allow for large plasma-free areas.

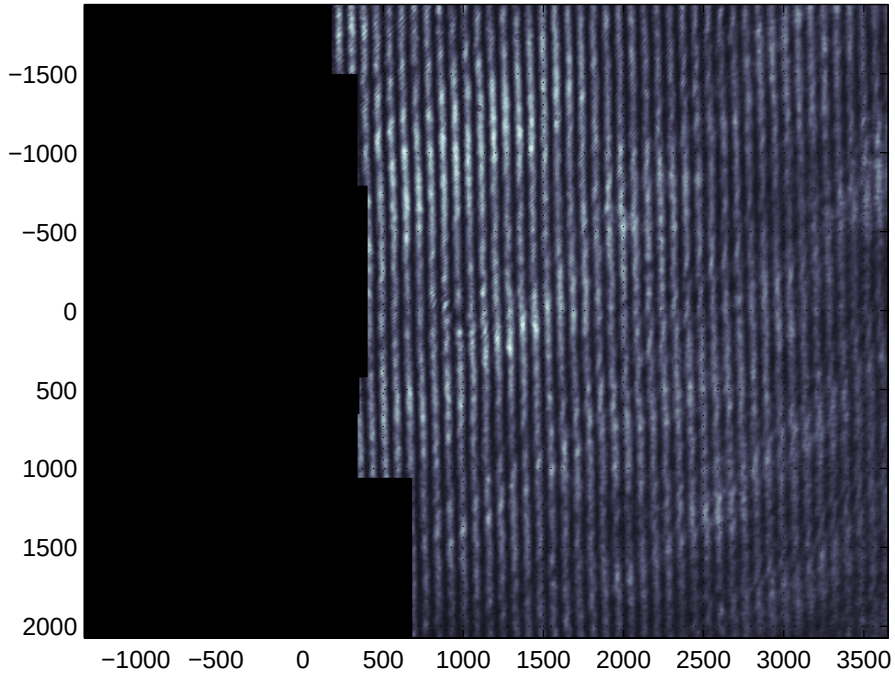

Figure 5.13: Reference image for the interferometry measurements, not calibrated (units are pixels)

First, the raw image is masked. Fig. 5.13 shows a reference image without the plasma. The target is on the left hand side of the image, already masked; the laser comes from the right, thus the plasma will expand from the target to the right hand side. Every area where there no fringes can be discerned has

to be masked, including the area where the target holder is located. Then, the image is processed in order to enhance the contrast between fringes. The enhanced image is made using a routine to process the image, however, if there are too many numerical artifacts this step can also be done manually, or the unprocessed image can be used if the contrast is high enough.

After this, the phase shift for each area is calculated using this contrast-enhanced image. From the phase shift, the electron density can be calculated. Fig. 5.14

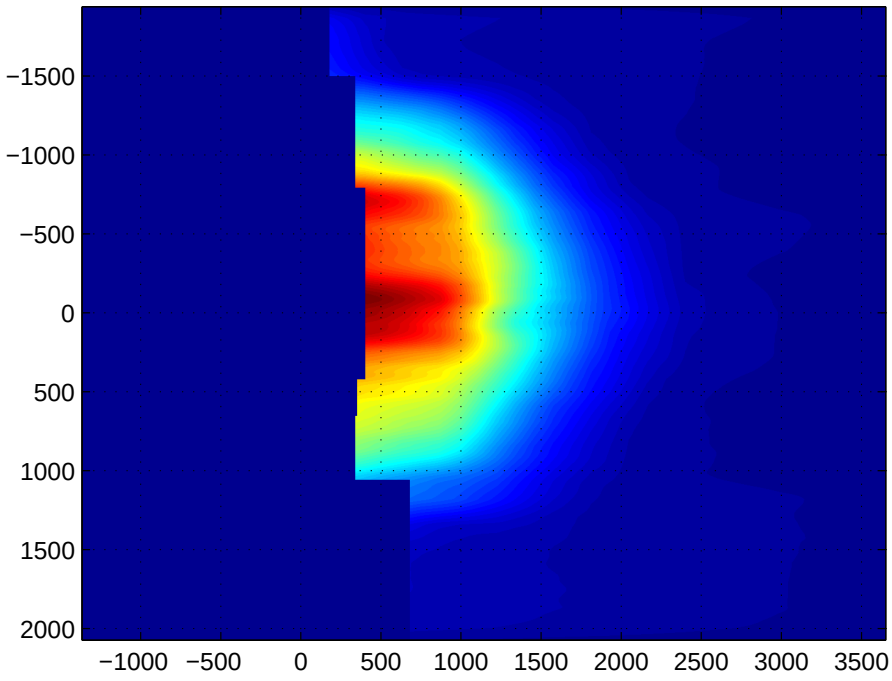

Figure 5.14: Calculated phase shift for the interferometry image

Finally, the energy loss of the ions is calculated in 2D using the free electron density information from the interferometry data. If there are numerical problems with the generated phase shift, there is also the option to use the unenhanced original image.

The electron density data obtained by using interferometry images has been compared to values obtained with the MIMOZA code. MIMOZA is a 2D hydrodynamic simulation code with radiation transport, developed by GSI collaboration partners in Sarov.

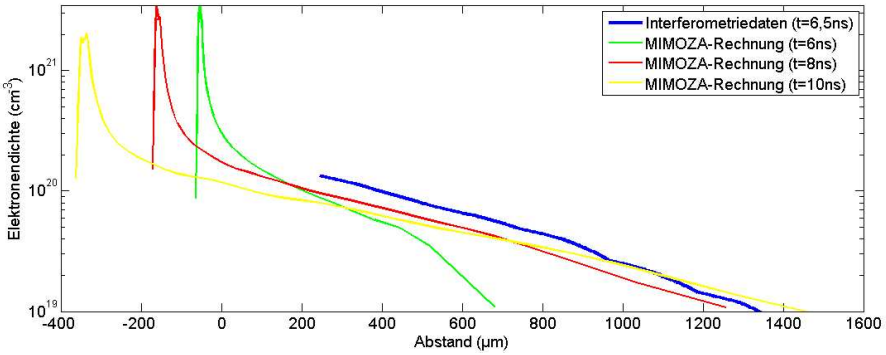

Figure 5.15: Comparison of electron density obtained with interferometry data (blue) with the MIMOZA code. Experimental data was taken at t=6.5 ns, MIMOZA values were calculated for t=6 ns (green), t=8 ns (red) and t=10 ns (yellow). [Fra08]

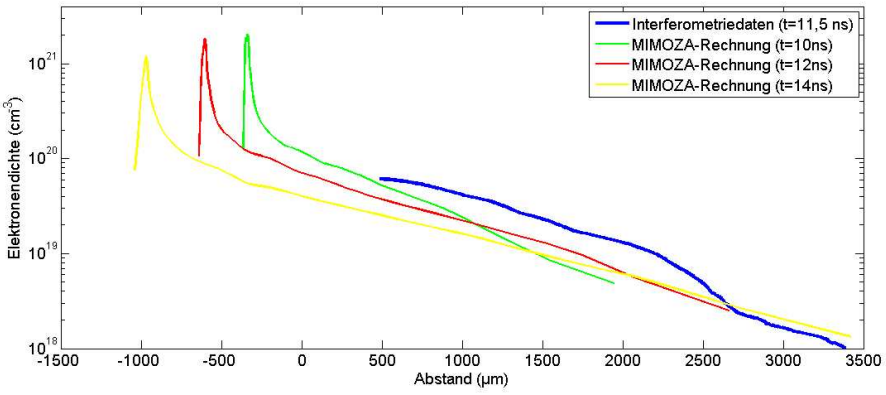

Figure 5.16: Comparison of electron density obtained with interferometry data (blue) with the MIMOZA code. Experimental data was taken at t=11.5 ns, MIMOZA values were calculated for t=10 ns (green), t=12 ns (red), and t=14 ns (yellow).[Fra08]

5.5 Measurements of transmitted light

One suggestion to explain the drop of the energy loss after the beginning of the laser irradiation was that maybe the foil first breaks into pieces due to the pressure of the laser before the pieces are turned into a plasma. Then the drop in energy loss would be explained by particles flying through gaps in between pieces of foil, before the plasma is fully formed.

To test this theory, a measurement of transmitted light was made. An Ulbricht integrating sphere was placed behind the target foil so that the light from the heating laser would reach the detector as soon as the foil became transparent for the laser light, see fig. 5.17. There was no ion beam, as only the interaction of the laser and the target foil were subject to investigation.

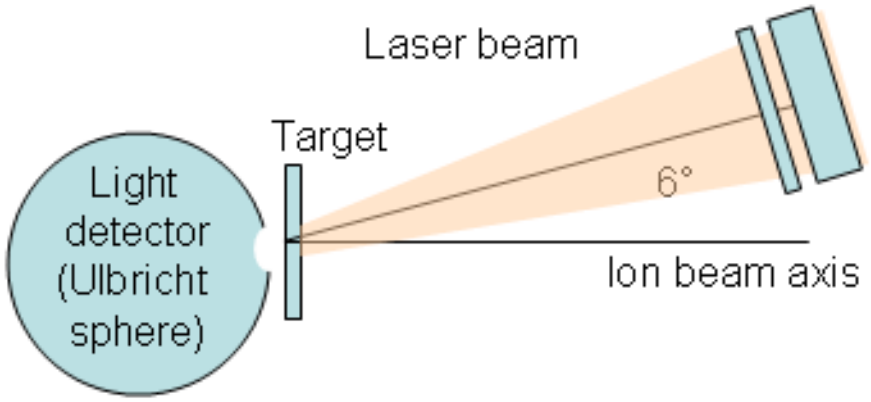

Figure 5.17: Experimental setup for the measurements of transmitted light using an Ulbricht integrating sphere.

A typical result of this measurement is shown in fig. 5.18. Here, the laser pulse and the Ulbricht sphere signal are shown together in the upper panel, while the lower panel shows the Ulbricht sphere signal alone.

All measurements made show that light only reaches the detector with the onset of the plasma, so any holes in the foil must be so small that even photons are unable to pass through them. This means that ions, who are much bigger, cannot pass through the foil either.

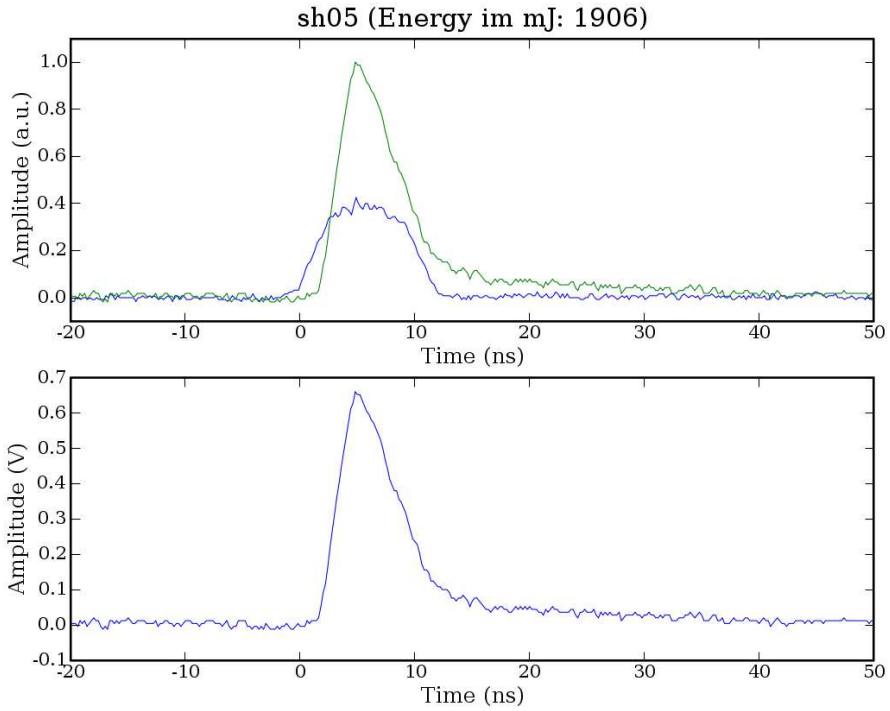

Figure 5.18: Measurement of transmitted light behind the target foil, using an Ulbricht sphere. The laser pulse is shown in blue in the top image. The bottom image shows the Ulbricht sphere signal only.

5.6 Particle loss

In the ongoing search for an explanation for the unexpected drop in energy loss obtained, it was speculated that particle loss between the target area and the detector could be responsible for the apparent loss in energy. If, in one particle bunch, particles with certain energies or charge states are scattered at an angle so that they do not reach the detector, this may result in an apparent decrease in energy loss. Energy loss is strongly dependent on the charge state of the ions. So, if higher charge states are scattered and lost, the peak of the resulting ion beam bunch will be shifted to the left. This would look like the ion beam bunch had experienced a decrease in energy loss, while in fact only the particles experiencing a higher energy loss are lost.

In order to further explore this topic, data from the 2006 experiments was also used. The data show that there is indeed a loss of particles, especially at the beginning of the laser pulse, as can be seen in fig. 5.19. Here, the

area of the ion pulse signals is calculated for each bunch, which corresponds to the number of particles. With the onset of the laser, each signal shows a drop, indicating loss of particles. While this affects only one of the bunches in the black measurement, the number of particles in the red measurement is reduced over several bunches.

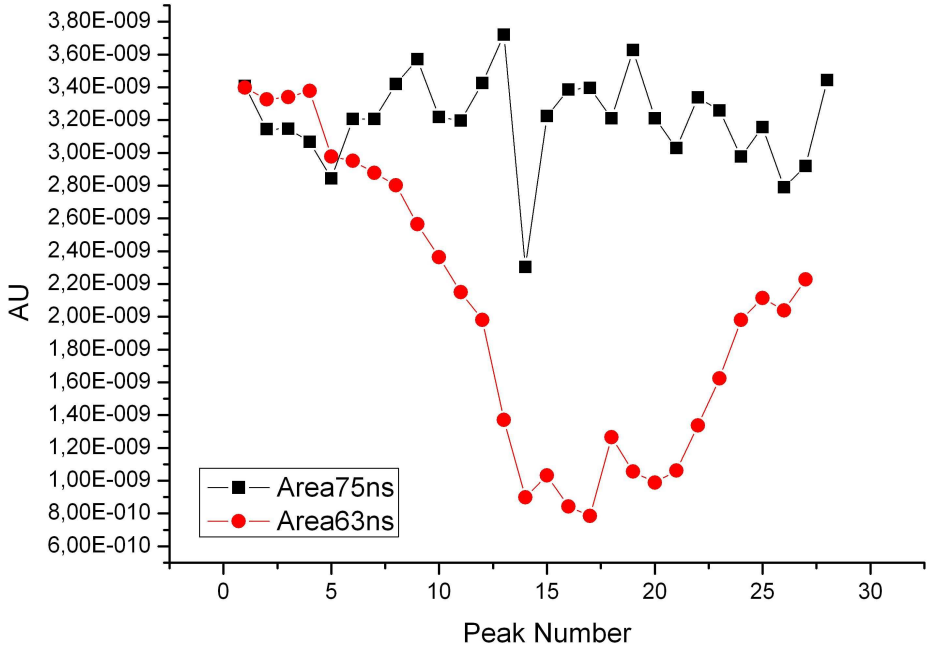

Figure 5.19: Comparison of the area of the ion bunch signals at two different laser-ion delays. The area corresponds to the number of particles in the bunch.

Chapter 6

Conclusions

Energy loss of ions in plasma is a matter very difficult to access experimentally, because so many parameters have to be controlled, and conditions in the extremely hot and dense center of plasmas will for a long time be accessible only to simulation. A simulation, however, needs to be based on a theory, and up to now there is no all-encompassing theory which takes into account all the different mechanisms of ion energy loss in plasmas.

For a long time, the modified Bethe-Bloch formula (eq. 2.16) has been considered the best description of the energy loss of ions in ionized matter, although it has its shortcomings. Even in this theoretical description, there are many parameters which are unknown.

A very important parameter is the free electron density, and it has been demonstrated that the interferometric method used in these experiments provides spatially resolved information about the electron density at least in the outer layers of the plasma region. However, the interferometry laser cannot penetrate through the innermost, hottest and densest region of the plasma at this frequency. Here, an increase in frequency might improve the situation, but the nhelix systems has its limits.

A promising approach is the work that has begun on the multi-frame interferometry. This was developed by A. Pelka, A.Schoekel and others, and if the method is improved, then it would be possible to obtain time-resolved and spatially resolved information on the free electron density, as interferograms could be taken at different times during the expansion of one plasma target.

Development of the new detector was a milestone in the energy loss measurements at Z6. With the new detector, data could be taken with the ECR ion source, thus the measurements have a much better time resolution. This is crucial since the plasma has a lifetime of about 20 ns, so all important processes take place on a nanosecond time scale. Another improvement is the

much lower signal-to-noise ratio of the new detector, which allowed us to use a 500μm aperture for the ion beam. Additionally, it is now possible to use thin 100 μg/cm^2 carbon foils as targets, where it has been shown that these are indeed completely transformed into plasma by the laser, so the target is completely in a plasma state and not in an intermediate, undefined stage as were the thicker foils used in previous experiments.

The error in determining the laser timing could be reduced by using two independent methods of measurement, the new method of direct measurement with a photo diode and the old method of indirect measurement using the X-ray flash of the plasma ignition. It has been shown that the results obtained differ very little from each other. Thus, the debate about whether the X-rays are indeed emitted at the very instant the laser hits the target or later can be laid to rest.

The drop in energy loss has yet to be fully explained. Since the principle of the energy loss measurement relies on the location of the ion bunch signal peaks, any shift in these peaks will result in a shift in the energy loss calculated. If, however, a bunch is severely distorted, this may also lead to a shift of the peak. From our measurements, it can be seen that particles are lost from the bunch, especially during the laser pulse. If the change in charge state of the ions is so substantial that the following focusing quadrupoles overfocus or underfocus, these particles will be lost, cf. sect. 5.6. This loss will most affect those particles with the biggest change in charge state, which are the particles experiencing the highest energy loss. So, if the particles with the highest energy loss suffer from the highest transmission losses due to wrongly focusing quadrupoles, the resulting ion signal will be distorted and the peak shifted towards less energy loss. This could be an explanation for the drop. This possibility is supported by the fact that the drop was observed mostly in measurements with the diamond detector, not always with the MSP detector. The MSP measurements also indicate particle loss, but the detection surface of the MSP is larger than that of the diamond detector, so the effect of selectively scattering particles with higher energy loss out of the detector range should be much more pronounced with the diamond detector.

Chapter 7

Outlook

There remains much to be researched. The changes in charge state of the ions is very important, especially in regard to an explanation of the drop in energy loss, and has not been subject to investigation since [Sue99]. A new ion detector will be capable of measuring the charge state distribution of an ion bunch after the flight through the plasma in another setup, which is currently past the planning and construction stage and has been used in first experiments by A.Frank and W. Cayzak.

If the scenario described in the previous chapter proves to be incorrect, another explanation will have to be found for the drop in energy loss.

The measurements made within the frame of this work also provide new experimental data for theories to be compared with. With this new data, theory groups will hopefully be able to produce new theoretical approaches on energy loss of ions in plasma, to replace the dated modified Bethe-Bloch formula.

Bibliography

[Beh98] T. Behnke et al., "The Charge Collection Properties of CVD Diamond", Nuclear Instruments and Methods in Physics Research A, Vol. 414, 340-356, 1998

[Bet30] H. Bethe, "Zur Theorie des Durchgangs schneller Korpuskularstrahlen durch Materie", Annalen der Physik 397, 325-400, 1930

[Bet83] H. D. Betz, "Applied Atomic Collision Physics", Vol. 4, p.1, Pure and Applied Physics 43-4, Academic Press, Orlando, 1983

[Blo33] F. Bloch, "Zur Bremsung rasch bewegter Teilchen beim Durchgang durch Materie", Annalen der Physik, 408: 285-320, 1933

[Boh13] N. Bohr, "On the theory of the decrease of velocity of moving electrified particles on passing through matter", Philos. Mag. 25:10-31, 1913

[Eli02] S. Eliezer, "The Interaction of High-Power Lasers with Plasmas", IoP Publishing, Bristol/Philadelphia, 2002

[For08] P. Forck, "Lecture Notes on Beam Instrumentation and Diagnostics", GSI/Joint Universities Accelerator School (JUAS), 2008

[GSI09] http://www-inj.gsi.de/

[Fra08] A. Frank, "Energieverlust von Schwerionenstrahlen in lasererzeugten Plasmen", diploma thesis, TU Darmstadt, 2008

[Hof94] D.H.H. Hoffmann et al, "Energy loss of fast heavy ions in plasmas", Nucl. Instr. Meth. B 90(1), 1994

[Hum99] S. Humphries Jr., "Principles of Charged Particle Acceleration", J. Wiley and Sons, 1986; internet version: http://www.fieldp.com/cpa/cpa.html (1999)

[Hum02] S. Humphries Jr., "Charged Particle Beams", J. Wiley and Sons, 1990; internet version: http://www.fieldp.com/cpb/cpb.html (2002)

[Jac98] J. Jacoby, "Untersuchungen der Eigenschaften von Materie bei hoher Energiedichte mit Ionenstrahlen", Habilitationsschrift, Friedrich-Alexander-Universität Erlangen-Nürnberg, 1998

[Jon09] B. Jones et al., http://meetings.aps.org/link/BAPS.2009.DPP.TO7.11

[Men01] R. Menzel, "Photonics", Springer-Verlag (2001)

[Mul73] P. Mulser et al., "Plasma Production by Laser", Physics Reports C, 3, 1973

[Mul07] P. Mulser, D. Bauer, "High Power Laser-Matter interaction," lecture notes, 2007

[Nis00] K. Nishikawa and M. Wakatani, "Plasma Physics", 3rd edition, Springer-Verlag (2000)

[Pel05] A. Pelka, "Bestimmung der Elektronendichte in lasererzeugten Plasmen mittels Laserinterferometrie", diploma thesis, TU Darmstadt, 2005

[Pet91] T. Peter and B. Kärcher, "Influence of partial ionization on the energy loss of fast ions in high-Z material", J. Appl. Phys., 69(7):3835 (1991).

[Ro97] M. Roth, "Experimentelle Bestimmung des Energieverlustes schwerer Ionen in lasererzeugten Plasmen", doctoral thesis, TU Darmstadt (1997)

[Sch07] G. Schaumann, "Experimente mit lasergeheizten Hohlräumen für die Untersuchung der Wechselwirkung von Schwerionen mit ionisierter Materie", doctoral thesis, TU Darmstadt (2007)

[Sch05] M. Schollmeier, personal communication, 2005

[Sch08] A. Schoekel, diploma thesis, TU Darmstadt, 2008

[Sue99] W. Süß, "Experimentelle Bestimmung der Ladungsverteilung Schwerer Ionen nach Wechselwirkung mit dichten, lasererzeugten Plasmen", doctoral thesis, TU Darmstadt (1999)

[Wam06] F. Wamers, "Entwicklung eines Detektors für gepulste Schwerionenstrahlen", diploma thesis, TU Darmstadt (2006)

[Zie03] J.F. Ziegler, "SRIM - The Stopping and Range of Ions in Matter", http://www.srim.org/ (2003/2008)

[Zie84] J.F. Ziegler, J.P. Biersack, U. Littmark, "The Stopping and Range of Ions in Solids", Vol. I of Series "Stopping and Ranges of Ions in Matter", Pergamon Press, New York (1984)

[Zil08] J. Zils, student project, unpublished, 2008.

Acknowledgments

Many people have contributed to this thesis in one way or another. Without them, this work would not have been possible.

I would like to thank Prof. Dr. Markus Roth for giving me the opportunity to write this thesis in the laser and plasma physics group at TU Darmstadt and for his continuing support and interest in my work.

I would like to thank Prof. Dr. D.H.H. Hoffmann for co-refereeing this thesis.

I would like to thank A. Blazevic, A. Frank, F. Wamers and A. Pelka for discussions and for their answers to many questions.

I would like to thank the entire plasma physics group of GSI and the laser and plasma physics group of TU Darmstadt for the enjoyable working atmosphere, for countless discussions and for their help with all kinds of problems.

I would like to thank Heinrich Wahl for his help with technical issues.

I would also like to thank the GSI workshop and the GSI target laboratory, especially Bettina Lommel.

I would like to thank John Rhys-Davies for the encouragement.

I would like to thank my parents, Rainer and Gisela Knobloch, for their constant support over the years.

And last but not least, I would like to thank my husband Axel Maas for all his love, support and patience.

Curriculum vitae

Name	Renate Knobloch-Maas, née Knobloch
Date of birth	Sep 20, 1976
Place of birth	Frankfurt am Main, Germany
Nationality	German
Address	Kelsterbacher Str. 16, 60528 Frankfurt, Germany
1976	Born as daughter of Rainer Knobloch and Gisela Knobloch, née Otto
1983-1987	Elementary school: Frauenhofschule in Frankfurt
1987-1993	High school: Gymnasium Schillerschule in Frankfurt
1993-1994	MMI Preparatory School in Freeland, Pennsylvania, U.S.A.
1994-1996	High school: Gymnasium Schillerschule in Frankfurt
1996	High school graduation with general qualification for university entrance (Abitur)
1996-2004	Study of physics at Darmstadt University of Technology, interrupted by chemotherapy
2004	University diploma in physics, equivalent to a master's degree (MSc)
2004-2009	Doctoral study of physics at Darmstadt University of Technology, 2004-2006 member of the scientific staff at the Institute for Nuclear Physics of Darmstadt University of Technology